On the Mapping of Multivariate Geophysical Fields: Sensitivities to Size, Scales, and Dynamics

P. F. J. LERMUSIAUX

Division of Engineering and Applied Sciences, Harvard University, Cambridge, Massachusetts

(Manuscript received 3 July 2001, in final form 8 February 2002)

ABSTRACT

The effects of a priori parameters on the error subspace estimation and mapping methodology introduced by P. F. J. Lermusiaux et al. is investigated. The approach is three-dimensional, multivariate, and multiscale. The sensitivities of the subspace and a posteriori fields to the size of the subspace, scales considered, and nonlinearities in the dynamical adjustments are studied. Applications focus on the mesoscale to subbasin-scale physics in the northwestern Levantine Sea during 10 February–15 March and 19 March–16 April 1995. Forecasts generated from various analyzed fields are compared to in situ and satellite data. The sensitivities to size show that the truncation to a subspace is efficient. The use of criteria to determine adequate sizes is emphasized and a back-of-the-envelope rule is outlined. The sensitivities to scales confirm that, for a given region, smaller scales usually require larger subspaces because of spectral redness. However, synoptic conditions are also shown to strongly influence the ordering of scales. The sensitivities to the dynamical adjustment reveal that nonlinearities can modify the variability decomposition, especially the dominant eigenvectors, and that changes are largest for the features and regions with high shears. Based on the estimated variability variance fields, eigenvalue spectra, multivariate eigenvectors and (cross)-covariance functions, dominant dynamical balances and the spatial distribution of hydrographic and velocity characteristic scales are obtained for primary regional features. In particular, the Ierapetra Eddy is found to be close to gradient-wind balance and coastal-trapped waves are anticipated to occur along the northern escarpment of the basin.

1. Introduction

In mapping geophysical fields and their uncertainties, it is important to assess the sensitivity to parameters. The present work carries out such studies for the a priori error subspace estimation and mapping methodology introduced in (Lermusiaux et al. 2000, henceforth LAL00). With this three-dimensional, multivariate, and multiscale approach (appendix A), the a priori error subspace, that is, the dominant components of the a priori missing variability or probability density functions of the state to be mapped, are constructed in two parts. The observed portions of the subspace are specified based on measurements and multiscale statistical models. The nonobserved portions are then built by dynamical adjustments to the observed portions. Once this a priori error subspace is computed, the datasets of interest can be mapped into gridded fields and error properties by Bayesian estimation in the subspace. Presently, error statistics are assumed to be described by covariance matrices and the mapping (analysis) reduces to a minimum error variance estimation problem. The subspace is then determined by the dominant eigendecomposition of the a priori error covariance.

Two main objectives are to investigate (i) the sensitivity of the state and error estimates to the properties of the subspace (e.g., size, dynamics, adjustment) and (ii) the sensitivity of the subspace itself to its size and to the data and dynamics utilized in its construction. The types of questions considered include: How many, and why so many, eigenvectors should be employed to represent most of a covariance matrix or to carry out a mapping? How sensitive is the subspace to the parameters of the model employed in its dynamical adjustment? By how much should such subspaces be dynamically adjusted? What is the performance of forecasts generated from these analyses? Results obtained from different a priori parameters are compared among each other and also to those of the univariate horizontal (2D) scheme of the Harvard Ocean Prediction System (HOPS; Lozano et al. 1996; Robinson 1996). Since this benchmark is multiscale, the present 3D mapping of fields and error covariances is referred to in short as the ''multivariate 3D'' scheme. Ultimately, forecasts generated from the various analyses are compared to in situ and satellite data, using root-mean-square differences and correlation coefficients for measures of skill. The

Corresponding author address: Pierre F. J. Lermusiaux, Division of Engineering and Applied Sciences, Pierce Hall G2A, Harvard University, 29 Oxford St., Cambridge, MA 02318.
E-mail: pierrel@pacific.harvard.edu

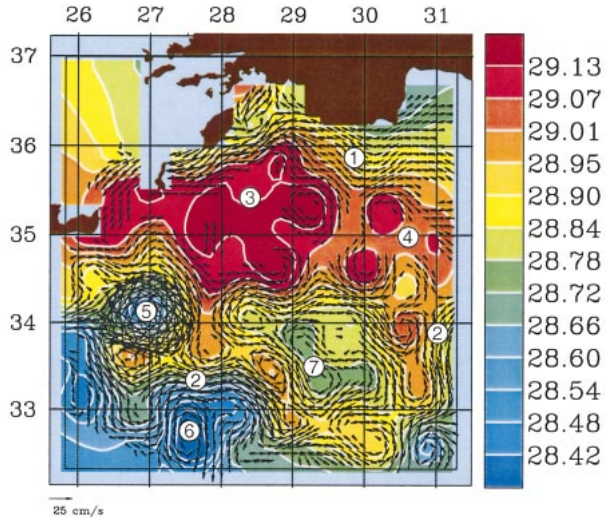

FIG. 1. For case 4 (see section 4), 27 Mar analysis (nowcast) of the potential density σ_θ at 105 m, overlaid with the horizontal velocity vectors at 5 m (vectors are plotted only if the analyzed $\|\mathbf{u}\|$ is larger than 6 cm s^{-1}). Numbers identify the location of the main upper-thermocline features: Asia Minor Current (1), Mid-Mediterranean Jet (2), Rhodes Gyre (3), West Cyprus Gyre (4), Ierapetra Eddy (5), a lobe of the Mersa Matruh Gyre (6), and main anticyclone in the Mersa Matruh-Shikmona Gyre complex (7). Several water masses of the Levantine are clearly visible. For the geography and bathymetry, see Fig. 8a of LAL00; for cartoons of the circulation, see Fig. 2 of Robinson and Golnaraghi (1993).

third objective is to extract dynamical knowledge from the variability subspaces and fields computed. This is carried out by studying the spatial distribution of the estimated hydrographic and velocity variances, shapes and amplitudes of dominant multivariate eigenvectors, and structures of (cross)-covariance functions.

The applications illustrated are in the Levantine Sea and focus on the mesoscale to subbasin-scale physical errors and fields. The measurements were collected during the LIW95 campaign (Roether et al. 1996; Malanotte-Rizzoli et al. 1996) carried out from January to April 1995 in the eastern Mediterranean. To introduce this region and its contemporary upper-thermocline features, a multivariate 3D estimate of the potential density at 105 m and velocity at 5 m is plotted in Fig. 1. Because of thermal-wind effects, several surface circulation structures are easily distinguished along the steepest slopes of isopycnals. To date, most investigations in the Levantine that combine data and dynamics have mainly resolved the subbasin scales and are usually based on close-to-geostrophy hypotheses (e.g., Hecht et al. 1988; Milliff and Robinson 1992; Özsoy et al. 1993; Robinson and Malanotte-Rizzoli 1993; Malanotte-Rizzoli et al. 1999).

Among the various techniques for the analysis of geophysical fields, only some estimate uncertainties (LAL00 and references cited therein). The present work is concerned with determining accurate a priori (error) covariance or structure functions and with estimating their parameters and covariance matrix form. Recent studies include: in atmospheric science, Rabier et al. (1998), Riishojgaard (1998), Dee and da Silva (1999), Gaspari and Cohn (1999), Gneiting (1999), Franke and Barker (2000); in physical oceanography, Cressie and Huang (1999), Miller and Cornuelle (1999), Menemenlis and Chechelnitsky (2000), Molinari and Festa (2000); and, in biological oceanography, Abbott and Letelier (1998). Today, error models, in particular the efficient representation of error covariance matrices, are essential for error predictions (Ehrendorfer 1997; Lermusiaux 1997, henceforth LER97) and data assimilation (Robinson et al. 1998; Chin et al. 1999; Derber and Bouttier 1999; Lermusiaux 1999a,b; Lermusiaux and Robinson 1999; Verron et al. 1999; Mitchell and Houtekamer 2000; Tippett et al. 2000; Hamill et al. 2001; Reichle et al. 2002).

In what follows, section 2 outlines a simple rule for estimating the size of error subspaces. In section 3, variations of these subspaces with their size and with the scales in the data, and the impacts of these variations on a posteriori fields, are illustrated for temperature and salinity. Section 4 proceeds to the complete physics: in addition to size and scales, nonlinear effects are studied and some dynamical properties derived. In section 5, the performance of forecasts initialized based on the present mapping is evaluated. Conclusions are in section 6. In the appendixes, algorithms are summarized and relevant nondimensional numbers listed.

2. The size of error subspaces: Back-of-the-envelope calculation

A simple rule giving an approximate order of magnitude for the size of multivariate error subspaces is outlined. It is based on experience with more quantitative calculations (e.g., Fukumori and Malanotte-Rizzoli 1995; LER97; Lermusiaux 1999a,b) and on the often red spectra of ocean phenomena. It is exemplified for the case where errors are mesoscale variability.

Consider first one state variable, for example, temperature or zonal velocity. For the vertical variability, two to three empirical orthogonal functions (EOFs) or dynamical modes often explain most of the significant variance (e.g., De Mey and Robinson 1987; Haney et al. 1995; De Mey 1997; Wunsch 1997; Pedder and Gomis 1998; von Storch and Frankignoul 1998). For the horizontal variability, most studies to date focus on surface fields. In that case, the number of dominant patterns or modes usually varies from 15 to about 50: for example, consider a surface field in the Gulf Stream or Atlantic region (e.g., Thacker and Lewandowicz 1996, 1997; Everson et al. 1997; Kaplan et al. 1997). For the 3D variability, an approximate subspace size is simply the product of vertical and horizontal requirements. With the above values, this product yields a size of 30–150.

In the case of several state variables, the size of the

subspace necessary to describe most of a normalized form of the multivariate variability is often found proportional to the number of variables. With this hypothesis, considering, for example, the primitive equation (PE) model[1] of HOPS and the above mesoscale values, an approximate size is then 135–650. This is of the order of 10^2 to 10^3. In summary, the order of magnitude of the size p of an error subspace is often well approximated by,

$$O(p) \simeq \sum_{v} n_h^v \times n_z^v, \tag{1}$$

where n_h^v (n_z^v) is an estimate of the horizontal (vertical) requirements for the state variable v. Similarly, a range of likely p is obtained from the products of the minimum and maximum horizontal and vertical requirements; that is, $\Sigma_v \min(n_h^v \times n_z^v) \leq p \leq \Sigma_v \max(n_h^v \times n_z^v)$. Such back-of-the-envelope rules do not require extensive 3D computations. They are very useful today since they provide quick estimates of the number of state samples, breed vectors, or singular vectors (e.g., Molteni et al. 1996; Toth and Kalnay 1997; Barkmeijer et al. 1998) needed to explain most of the variance in an analysis or ensemble forecast.

The above sizes are much larger than classic 1D requirements but much smaller than the number of discrete state variables. For example, consider a nondimensional (from here on denoted by *) covariance matrix $\mathbf{B}^*$ for a horizontal, univariate field. For covariance function, we use a ''Mexican hat''[2] and for discretized domain, the northwestern Levantine with a uniform resolution of 10 km (500 km in the x and 520 km in the y direction). The size of $\mathbf{B}^*$ is thus (2703×2703). Computing its cumulative eigenvalue spectrum for the subbasin-scales (200-km zero crossing, 100-km decay scale), 15 eigenvectors represent 85% of the variance, 36 vectors 99%, and 50 vectors 99.8%. For the mesoscales (60-km zero crossing, 30-km decay scale), larger numbers are required: 15 eigenvectors represent 20% of the variance, 50 vectors 56%, and 100 vectors 83%. For at least 90% of the variance, 19 vectors are necessary for the subbasin-scales and 128 for the mesoscales. These sizes represent only 0.7% and 4.7% of the number of discrete state variables, 2703, respectively. Illustrations and further details are in LLA98.

3. Multivariate three-dimensional analysis of tracer fields: Subspace size

Hydrographic data (dynamical tracers T and S) are frequent observations. The sensitivity of the a posteriori state $\mathbf{x}_{\text{trc}}^a$ to the size of the a priori error subspace is thus first exemplified for the case of a global mapping of temperature and salinity. The subspace is constructed assuming that the a priori error covariance of these tracers $\mathbf{B}_{\text{trc}}$ is ''observed'' in the sense of LAL00, that is, historical (synoptic) data are available to specify its dominant eigendecomposition $\mathbf{B}_{\text{trc}}^p$. Variations of $\mathbf{B}_{\text{trc}}^p$ with the scales considered are illustrated. Some differences between our multivariate 3D scheme and Kalman update (appendix A section c) are also exemplified.

The data are 146 T and S profiles (Figs. 2a,b). Their error model (appendix A) includes a decorrelation time term. The numerical domain (Fig. 2c) contains 2703 horizontal grid points and 20 vertical levels (108 120 tracer state variables). There are 5840 data points [dimension of $\mathbf{y}^o$, Eq. (A1b)], that is, the number of T, S scalar data residuals on vertical levels.

The benchmark univariate 2D scheme of HOPS assumes that two independent scales are present and that errors are homogeneous horizontally. It uses a successive correction, minimum error variance technique (e.g., Daley 1991; Lorenc 1992): the largest scales are gridded first and the resulting fields constitute the background in the mapping of smaller scales. Successively for each scale, global horizontal analyses of scale-filtered T and S data are thus carried out at various levels. For fair comparisons with this benchmark, the present multivariate 3D scheme is also a two-scale correction ($w = 1, 2$ in appendix A sections b–c), with horizontally homogeneous a priori errors. It thus carries out two multivariate 3D mappings successively. For each scale, $\mathbf{B}_{\text{trc}}^p$ is constructed based on a statistical model fit to data in the horizontal and on data EOFs in the vertical [appendix A section b(1)]. In this section, the data used to do so is $\mathbf{y}^o$. For both schemes, the first a priori estimate $\mathbf{x}_{\text{trc}}^b$ ($w = 0$ in appendix A sections b–c) is the horizontal average of $\mathbf{y}^o$. Subsequently, the two scales are the subbasin-scale and mesoscale. At the mesoscale stage (section 3b), a priori errors are mesoscale variability but a posteriori fields are the total fields.

a. Subbasin scale

UNIVARIATE 2D BENCHMARK: Figure 3 shows four subbasin-scale ($w = 1$) univariate 2D analyses. The a priori horizontal covariance was set to be a ''Mexican hat'' (section 2) of 200-km zero crossing and 100-km decay scale, each estimated based on covariances among subbasin-scale data residuals. The data error covariance at data points was assumed diagonal (at each level, $\mathbf{R}$

[1] This dynamical PE model governs five state variables, henceforth called the PE fields: four 3D fields, the temperature T, salinity S, and internal horizontal velocities $\hat{u}$ and $\hat{v}$ (zonal x and meridional y directions), and one 2D field, the barotropic transport streamfunction ψ. The main model parameters are in Lermusiaux et al. (1998, henceforth LLA98).

[2] This is the negative of the second derivative of a 2D Gaussian function (e.g., Carter and Robinson 1987; Louis et al. 1997). Parameters are the zero crossing l_a, e-folding decay scale l_b, and decorrelation time τ. Elements of $\mathbf{B}^*$ are of the form $C^*(\mathbf{r}_1, \mathbf{r}_2) = (1 - a^2)e^{-b^2/2}$, where $a^2 = (\mathbf{r}_1 - \mathbf{r}_2)^T \mathbf{L}_a^{-2}(\mathbf{r}_1 - \mathbf{r}_2)$ and $b^2 = (\mathbf{r}_1 - \mathbf{r}_2)^T \mathbf{L}_b^{-2}(\mathbf{r}_1 - \mathbf{r}_2) + (\Delta t_i/\tau)^2$ are scalars, and $\mathbf{r}_1$ and $\mathbf{r}_2$ horizontal position vectors, with $\mathbf{r} = (x, y)$. The 2-by-2 matrix $\mathbf{L}_a$ contains l_a on its diagonal; $\mathbf{L}_b$ contains l_b. The decorrelation time term, in which Δt_i is the interval between the data time t_i and estimation time t_0, is part of the measurement error model (appendix A).

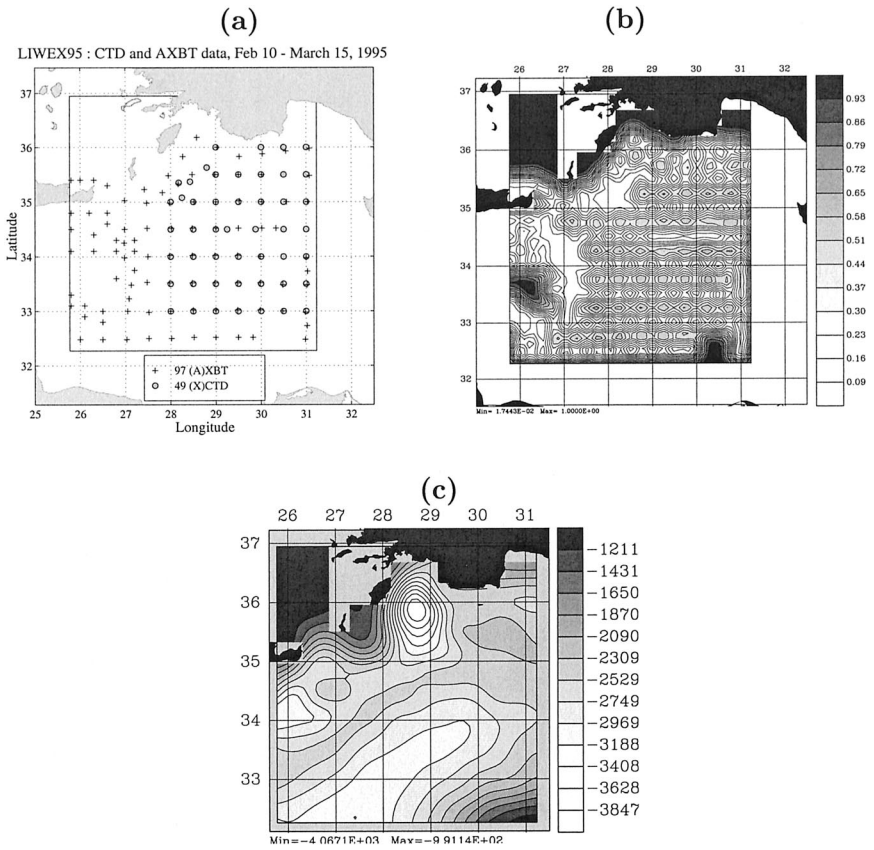

FIG. 2. (a) Coordinates of 146 hydrographic profiles that form $\mathbf{y}^o$ (appendix A) in the mappings of section 3. They originated from CTD and aircraft XBT observations gathered during 10–18 Feb and on 15 Mar 1995, respectively. (b) Surface (5 m) a posteriori mesoscale error variance for temperature, as estimated by the univariate 2D scheme. Errors are normalized (0–1) and computed using a ''Mexican hat'' for a priori covariance function (60-km zero crossings, 30-km decay scales) and an a priori error variance of uniform amplitude 1. (c) Model bottom topography (m) at tracer grid points.

$= r\mathbf{I}$) and of 50 days decorrelation timescale. The corresponding horizontally uniform, nondimensional (0 to 1) variance was calibrated to $r^* = 0.03$, mainly based on experience.

MULTIVARIATE 3D SCHEME: Figure 4 illustrates the construction of $\mathbf{B}_{\text{trc}}$ and Fig. 5 the mappings. The dominant eigendecomposition of $\mathbf{C}^z_{\text{trc}}$ [Eq. (A10)] is computed based on the EOFs of the subbasin-scale data residuals [Eqs. (A7)–(A9)]. A small number of *T, S* EOFs explains most of the variance (Fig. 4a). The horizontal covariance $\mathbf{C}^{r^*}_{\text{trc}}$ [Eq. (A11)] is analytical, computed based on the subbasin-scale Mexican hat used in the univariate 2D analyses. From Eqs. (A13)–(A15), the vertical [Eq. (A10)] and horizontal [Eq. (A12)] decompositions are then combined. The resulting normalized variance is explained by a few hundred 3D vectors (Fig. 4b). Using Eq. (A16) in (appendix A section c), the subbasin-scale mapping ($w = 1$) is finally carried out.

Figure 5a plots parts of the state $\mathbf{x}^a_{\text{trc}}$ for the case where $p = 500$ in Eq. (A16), that is, 500 eigenvectors are used, which explains 99.6% of the a priori error variance (Fig. 4b). The size of $\mathbf{x}^a_{\text{trc}}$ being 108 120, this analysis is 216 times cheaper than a full covariance formulation and about 12 times cheaper than a representer method (Bennett and Chua 1994), the number of representers being 5840. Comparing results (Figs. 5a and 3), the *T, S* maps are alike. For the subbasin scale, assuming zero vertical covariance and uncorrelated *T* and *S* error fields does not appear damaging. This is mainly because there is here more than enough data coverage for the subbasin scale. The vertical and *T*–*S* correlations are as expected stronger with the 3D scheme (Fig. 5a), but most differences are within data error bounds.

Comparing the *T, S* maps using 500 and 250 vectors (not shown), the relative root-mean-square (rms) differences are less than 1%. This is an interesting result. Once most (e.g., here $\geq$98%, see Fig. 4b) of the covariance has converged, the remaining eigenvectors can be ignored if their eigenvalues are negligible in comparison to data error eigenvalues (LLA98). Considering costs, the mapping with $p = 250$ is 10^3 times cheaper than the full covariance mapping. Finally, using 10 vec-

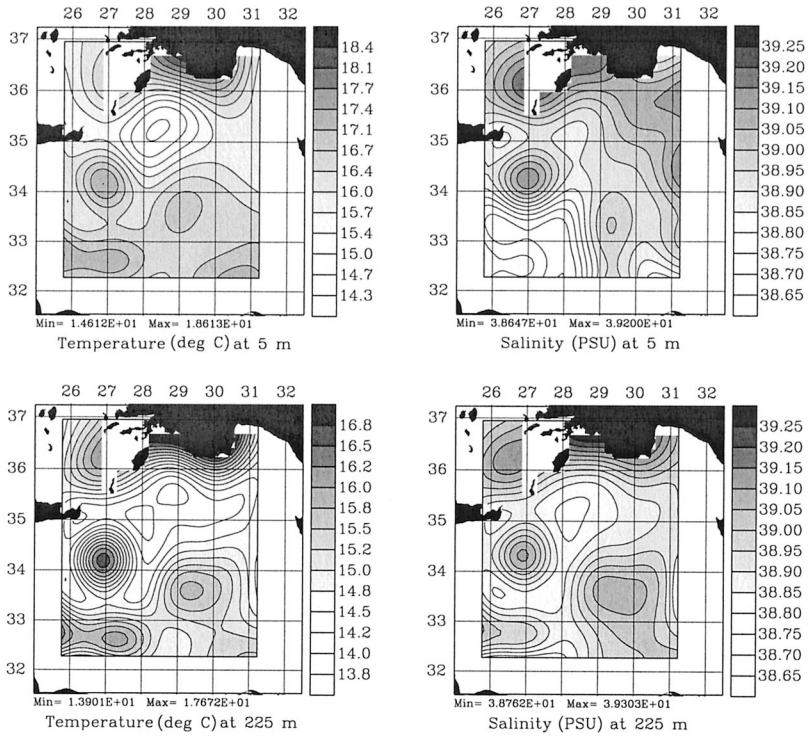

FIG. 3. Subbasin-scale ($w = 1$) temperature and salinity fields, at 5 and 225 m, as estimated by univariate 2D HOPS analyses. The scaling for temperature at 5 m differs from that at 225 m. The scaling for salinity is uniform with depth.

tors as on Fig. 5b is not sufficient. Indeed, the quick product of horizontal and vertical requirements for 99% of the variance each indicates here a total of $36 \times 8 = 288$ vectors [see Eq. (1) and use numbers in section 2 and Fig. 4a]. This back-of-the-envelope order of 10^2 multivariate 3D vectors agrees with the numerically computed spectra of Fig. 4b.

b. Mesoscale

UNIVARIATE 2D BENCHMARK: Figure 6 shows four mesoscale ($w = 2$) univariate 2D analyses. Based on plots of covariances among data residuals, the zero crossing was set at 60 km, decay scale at 30 km, and decorrelation timescale at 7 days. Other parameters are as in section 3a.

MULTIVARIATE 3D SCHEME: In the mesoscale 3D mapping, $\mathbf{x}^b_{\text{trc}}$ is the subbasin-scale state (Fig. 5a). The construction of the mesoscale $\mathbf{B}_{\text{trc}}$ is illustrated by Fig. 7. In the vertical (Fig. 7a), the variance of the mesoscale data residuals [Eq. (A10)] decays less rapidly with the eigenvalue number than in the subbasin-scale case (Fig. 4a). In the horizontal, $\mathbf{C}^{r^*}_{\text{trc}}$ [Eq. (A11)] is computed based on the mesoscale Mexican hat of the univariate 2D analyses. From Eqs. (A13)–(15), the vertical [Eq. (A10)] and horizontal [Eq. (A12)] decompositions are then combined. The resulting normalized mesoscale variance (Fig. 7b) is mostly explained by a few 3D vectors, but compared to the subbasin-scale (Fig. 4b), slightly more vectors are needed. Using Eq. (A16) in (appendix A section c), the mesoscale mapping ($w = 2$) is finally carried out.

Figures 8a–b show $\mathbf{x}^a_{\text{trc}}$ obtained using the dominant 500 and 750 mesoscale vectors, respectively. Differences with the fields of Fig. 6 are small, at several locations within data error bounds. However, the 3D scheme that uses the significant EOFs of the mesoscale residuals [Eqs. (A7)–(A10)] yields larger vertical correlations. For example, in the upper 0–50 m mixing layer, the measurement noise and unresolved vertical scales are filtered more on Figs. 8a–b. Small middepth features of significant vertical extension, for example, see *T, S* around 225 m, also seem better represented. For mesoscale mappings with data resolutions similar to those of Fig. 2a, a disadvantage of the univariate 2D analysis is in fact its sensitivity to environmental noise. Considering subspace sizes, the relative rms differences between maps of Figs. 8a and 8b are less than 3%. Even though 750 vectors explain 5% more a priori mesoscale variance than 500 vectors do (Fig. 7b), most of the additional 250 vectors have eigenvalues smaller than the local data error variance. They thus mainly yield mesoscale corrections within data error bounds.

For the 3D scheme, two main properties have been exemplified. First, once most of the a priori error covariance has converged (e.g., 99%), the remaining ei-

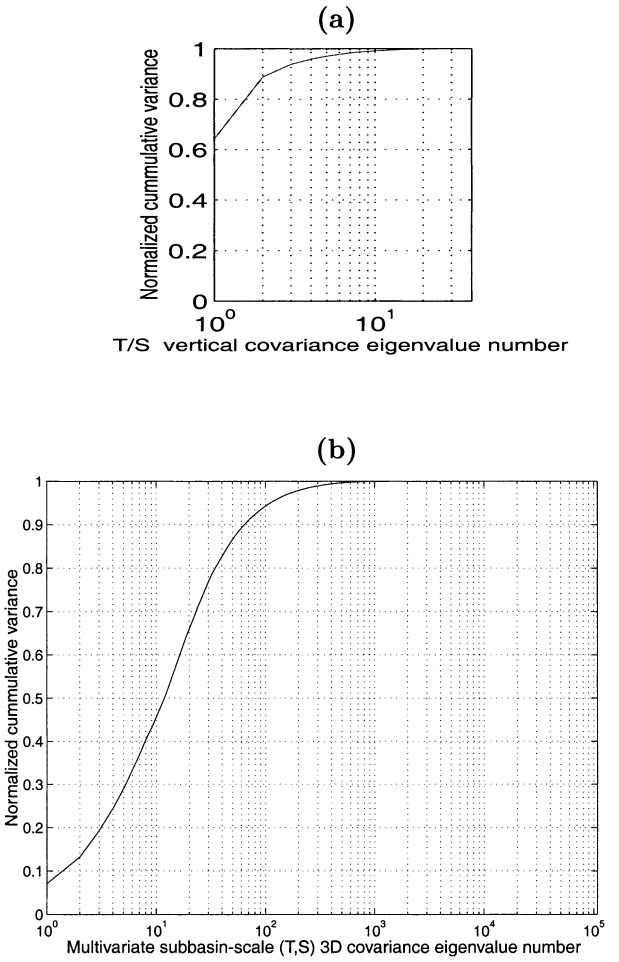

FIG. 4. (a) Normalized cumulative variance of the subbasin-scale residuals of the tracer profiles, as a function of the eigenvalue number. The covariance $\mathbf{C}^z_{\text{trc}}$ is (40 × 40). The first *T, S* vertical EOF explains 64% of the subbasin-scale variance, the second 25%, third 5%, and fourth 2%. They account together for 96% of the variance; the dominant eight for 99%. (b) Normalized cumulative variance of the subbasin-scale error covariance of the 3D tracer fields, $\mathbf{B}_{\text{trc}}$ [Eq. (A13)], as a function of the eigenvalue number. The size of $\mathbf{B}_{\text{trc}}$ is (108120 × 108120). The dominant 10 eigenvectors explain 46% of the variance; the dominant 100, 94.25%; dominant 250, 98.5%; and dominant 500, 99.6%. Employing 100 instead of 108 120 vectors reduces complexity by more than 10^3 while only missing 6% of the variance.

genvectors can be truncated in most cases. Second, the a priori error vectors of eigenvalues negligible with respect to data errors have negligible impacts on the a posteriori state. Even if the a priori error covariance has not converged, these vectors can usually be omitted.

4. Multivariate three-dimensional analyses of PE fields

Primitive equation fields and errors are now considered. Examples remain in the northwestern Levantine, but the period is now 19 March–16 April 1995. Four cases are discussed (Table 1): one univariate 2D benchmark and three variations of the multivariate 3D scheme.

The univariate 2D benchmark (case 1) first carries out horizontal analyses for *T* and *S*, as in section 3. Total velocity is then computed by assuming geostrophic balance with the gridded tracers and integrating the thermal wind equations up and down from a level of reference.

The present multivariate 3D scheme (cases 2–4) again uses a two-scale approach ($w = 1, 2$ in appendix A section b) to construct the a priori error subspace. For each scale, the tracer portion $\mathbf{B}_{\text{trc}}$ of the a priori error covariance $\mathbf{B}$ is specified as in section 3. The nonobserved velocity portions are then built in dynamical accord with $\mathbf{B}_{\text{trc}}$, through an ensemble of adjustment momentum integrations (tracers are kept fixed in these adjustments [see appendix A section b(2)]. These integrations lead to an ensemble of PE adjusted fields. Variability samples, that is, the differences between these fields and a priori state $\mathbf{x}^b$, are then computed, normalized, and organized by singular value decomposition (SVD). Once a convergence criterion determines that the number of samples is large enough to explain most of the variance, an estimate $\mathbf{B}^p$ of $\mathbf{B}$ is obtained. A mapping (appendix A section c) is then carried out.

The 3D cases of Table 1 were selected to illustrate the main tendencies in an extensive set of computations. They exemplify the sensitivities of the error subspace and state $\mathbf{x}^a$ to: (i) the nonlinear terms of the momentum equations used to adjust the nonobserved velocity variability to the observed tracer variability (cases 2 and 3), and (ii) the size of the subspace p (cases 3 and 4). Subbasin-scale estimates are only overviewed (section 4a). Mesoscale estimates are studied in more detail: a priori error covariances $\mathbf{B}^p = \mathbf{E}\mathbf{\Pi}\mathbf{E}^{\text{T}}$ (section 4b), a posteriori fields (section 4.3), and a posteriori error covariances $\mathbf{B}^{a\,p} = \mathbf{E}^a\mathbf{\Pi}^a\mathbf{E}^{a^{\text{T}}}$ (section 4d). The dynamical possibilities raised by the study of subspaces are emphasized in sections 4b and 4d.

a. Subbasin scale

In each case (Table 1), the data $\mathbf{y}^o$ employed for the subbasin-scale are 512 profiles of the Mediterranean Ocean database (MODB) winter climatology for the Levantine (Brankart 1997, personal communication) and the *T–S* profiles for 10–18 February and 15 March (Fig. 2a). For coherence with the recent evolution of deep eastern Mediterranean waters (Roether et al. 1996), the MODB data were cut at 1250-m depth: only in situ data are utilized below 1250 m. In all cases, $\mathbf{x}^b$ is in hydrostatic equilibrium: its tracer fields are the horizontal averages of the data $\mathbf{y}^o$ and its velocity is null.

For the univariate 2D scheme (case 1), *T* and *S* fields are estimated from $\mathbf{y}^o$ as in section 3a. Total velocities are assumed in geostrophic balance, with a level of no motion at 600 m. For the multivariate 3D cases 2–4, the $\mathbf{B}^p_{\text{trc}}$'s are also as in section 3a, except for the different sizes p. Three estimates of the subbasin-scale $\mathbf{B}^p$ are then built using the PE model, as indicated in Table 1.

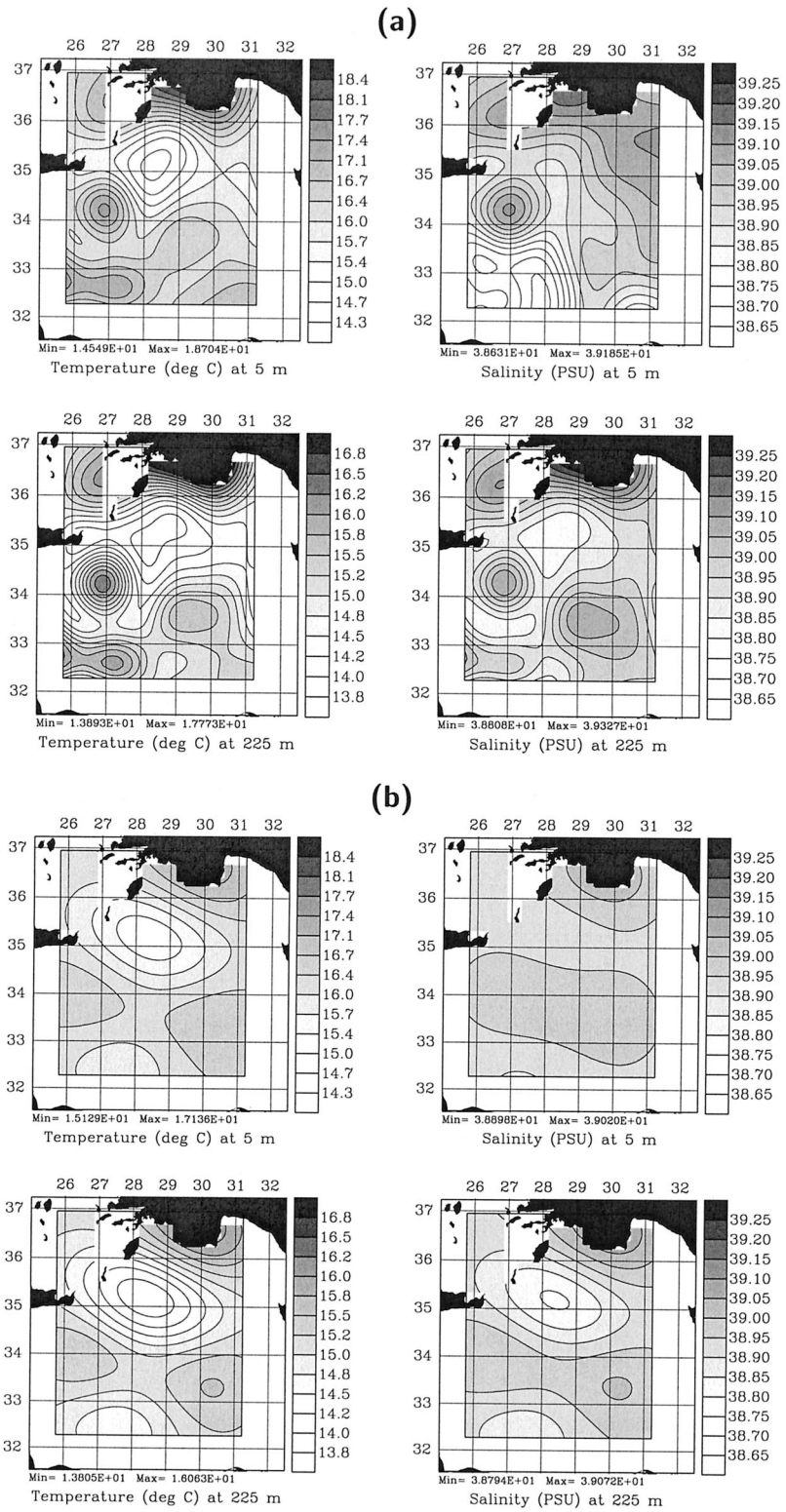

FIG. 5. (a) Subbasin-scale ($w = 1$) temperature and salinity fields, at 5 and 225 m, as estimated by a multivariate 3D error subspace analysis. The dominant 500 vectors of $\mathbf{B}_{trc}$ are used [Eq. (A16)]. Scalings and levels shown are as on Fig. 3. (b) As (a) but with the dominant 10 vectors of $\mathbf{B}_{trc}$.

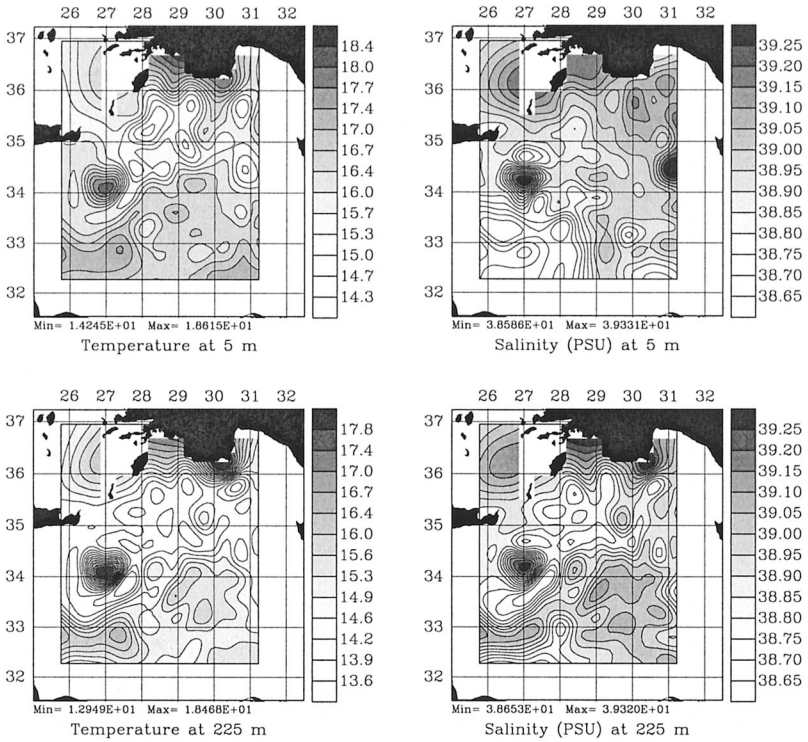

FIG. 6. Total (subbasin-scale plus mesoscale) *T* and *S* fields at 5 and 225 m, as estimated by univariate 2D HOPS analyses. The a priori estimate $\mathbf{x}^b_{\text{trc}}$ in this second stage ($w = 2$) is the subbasin-scale analysis of the first stage ($w = 1$) (see Fig. 3). For temperature, the scaling at 5 m differs from that on Fig. 3; for salinity, it is the same.

With these $\mathbf{B}^p$'s, three mappings of the data $\mathbf{y}^o$ are carried out, following (appendix A section c).

b. Mesoscale: Data and a priori error covariance

For each case (Table 1), the data for the mesoscale correction are 236 CTD profiles gathered from 19 March to 16 April (Fig. 9). They lead to 9440 data points (dimension of $\mathbf{y}^o$). To have an acceptable synoptic coverage (see section 5), the field estimation is centered on 27 March. The data decorrelation timescale is adjusted to 7 days.

The four $\mathbf{x}^b$'s (cases 1–4) are the four subbasin-scale fields of section 4a. Their a priori error is thus mesoscale variability: that is, for cases 2–4, $\mathbf{\Gamma} = \mathbf{I}$ in Eq. (A23). The corresponding covariances are computed using all 289 CTD profiles gathered from 10 February to 16 April (denoted by $\mathbf{y}^o_{\text{ctd}}$). These four covariance estimations are now described.

UNIVARIATE 2D BENCHMARK: Based on plots of covariances among mesoscale residuals of the 289 CTD, the zero crossing, decay scale, and data decorrelation timescale are adjusted on basin average to 60 km, 30 km, and 7 days. Other parameters of the error covariance function for *T* and *S* (see Fig. 9b) are as in section 3a. Velocity error covariances are not computed.

MULTIVARIATE 3D SCHEME: In constructing the mesoscale $\mathbf{B}^p = \mathbf{E}\mathbf{\Pi}\mathbf{E}^{\text{T}}$, the dominant decomposition of its tracer submatrix, $\mathbf{B}^p_{\text{trc}} = \mathbf{E}_{\text{trc}}\mathbf{\Pi}_{\text{trc}}\mathbf{E}^{\text{T}}_{\text{trc}}$, is computed first [appendix A section b(1)]. This is done by combining the vertical EOFs of the mesoscale tracer residuals [$\mathbf{y}^o_{\text{ctd}_i} - \mathcal{H}_i(\mathbf{x}^b)$, $i = 1, \ldots, 289$, Eq. (A7)] with the eigendecomposition of an analytical horizontal tracer covariance (of elements specified using the mesoscale Mexican hat of the benchmark). The resulting cumulative error variance is a curve similar to that of Fig. 7b. For the sizes p utilized (Table 1), the dominant 322 tracer eigenvectors explain 67.2% of the total tracer variance, the dominant 400, 72%, and dominant 500, 76.5%. The complete $\mathbf{B}^p$'s are then obtained from $\mathbf{B}^p_{\text{trc}}$, by adjustment momentum integrations [appendix A section b(2)]. The $j = 1, \ldots, p$ dynamical adjustments lasted for 2 model days, with p increasing based on the convergence criterion $\rho \geq \alpha$ [Eq. (A22)], with the limit α set to 0.93. This coefficient $\rho \leq 1$ assesses the added value of new parallel batches of adjustment runs; some of its values are listed in Table 2a. For case 2, $\rho \geq \alpha$ was achieved after 322 runs, for $p = 322$ and $\tilde{p} = 288$. For case 4, 400 runs were necessary, based on $p = 400$ and $\tilde{p} = 360$. This larger dimension is due to the nonlinear momentum terms that create flow variability not estimated by the linear adjustments of case 2. Since case 3 is simply the nonlinear extension of case 2, convergence is not an objective. Overall, the rate of increase of ρ diminishes as

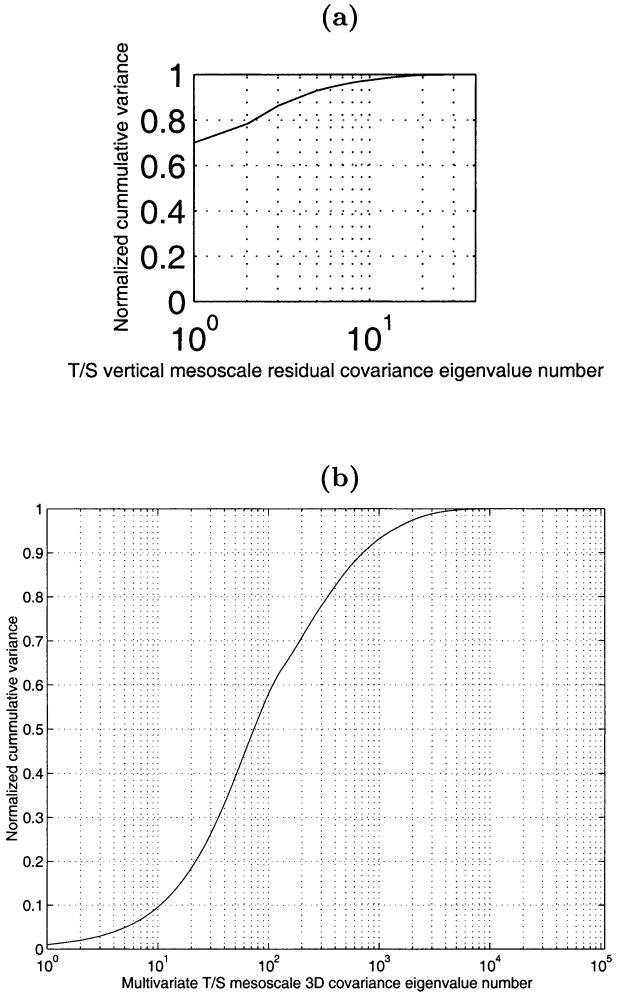

FIG. 7. (a) As for Fig. 4a but for the mesoscale residuals of the tracer profiles. The first *T, S* vertical EOF explains 70% of the mesoscale variance, the second 8%, third 7%, and fourth less than 4%. (b) As for Fig. 4b but for the mesoscale error covariance of the 3D tracer fields, $\mathbf{B}_{\text{trc}}$ [Eq. (A13)]. The dominant 100 eigenvectors explain 58% of the variance; the dominant 250, 75%; dominant 500, 86%; and dominant 750, 90.5%.

$\tilde{p} \leq p$ grows: this is partly because the singular values of $\mathbf{B}$ decay rapidly.

Table 2b estimates the overall similarity among the three $\mathbf{B}^p$'s, using Eq. (A22). Comparing cases 2 and 3, averaged on volume and state variables, nonlinear momentum terms only change about 2.7% of the nondimensional PE mesoscale variability. Since here $\mathbf{u}^j = \sqrt{p}\mathbf{e}^j$ in Eq. (A17), the tracer covariance in a $\mathbf{B}^p$ is exactly $\mathbf{B}^p_{\text{trc}}$. Therefore, the covariances involving total velocities in cases 2 and 3 differ by about $(1 - \rho)n/n_{\text{vel}} = 5.4\%$, where n is the state vector size (218 943) and n_{vel} the number of velocity variables (110 823). This 5.4% difference measures the volume-averaged effect of nonlinear momentum terms on velocity covariances. Comparing cases 3 and 4, they are about 13.2% apart. The tracer eigenvectors of high number (small eigenvalues) here affect velocity covariances.[3] Finally, comparing cases 2 and 4, their differences combine the nonlinear and size effects (2.7% and 13.2%).

The three $\mathbf{B}^p = \mathbf{E\Pi E}^{\text{T}}$'s (cases 2–4) are now compared locally, focusing on variances [section 4b(1)], eigenvectors [section 4b(2)] and covariance functions [section 4b(4)]. These estimates substantially improve the univariate 2D scheme, which only provides 2D error variance fields.

1) A PRIORI MESOSCALE ERROR VARIANCE

Univariate 2D benchmark: A priori tracer error variances are set to the horizontally averaged variance of the residuals of $\mathbf{y}^o_{\text{ctd}}$: they are depth dependent. The corresponding velocity error variances are set assuming geostrophic balance.

Multivariate 3D scheme: Error variances form the diagonal of the $\mathbf{B}^p$'s. Tracer variances are horizontally uniform in the data domain (Fig. 9). For cases 2 and 3 ($p = 322$), the *T–S* error standard deviation at 5 m is 0.40°C/0.080 PSU, while at 500 m, it is 0.17°C/0.039 PSU. For case 4 (see LAL00), standard deviations are logically slightly larger: to first order[4], using the variance numbers given above, by 3.3%–3.6% [$100 \times (72 - 67.2)/2$, divided by 72 and 67.2]. Total velocity variances are nonuniform in 3D. By construction, large a priori errors (Table 3) correspond to the locations and features estimated to have large mesoscale flow variability. They reflect local variations of the dominant density and momentum balances.

In case 2 (linear momentum), at the surface, the largest standard deviations are as expected above the Rhodes Basin (flanked by steep topography) within the deep, subbasin-scale Rhodes Gyre. Other features of above-average flow variability are, in decreasing order, the Ierapetra, Mersa Matruh Gyre (one of its lobes is in the domain) and central branch of the Mid-Mediterranean Jet. At 500-m depth, the largest $\hat{u}$, $\hat{v}$ deviations are near the inflow/outflow of the Kasos and Karpathos Straits, and again above the Rhodes Basin.

In case 3 (nonlinear momentum, $p = 322$), at the surface, it is now the high-velocity, small size Ierapetra that dominates. The correction to the larger Mersa Matruh Gyre is smaller, especially in ψ. For the subbasin-scale Rhodes Gyre and Mid-Mediterranean Jet, nonlinear terms only have a small impact. At 500-m depth, the two Straits and Rhodes Basin still dominate internal deviations, but case 3 also estimates that the Ierapetra and an anticyclone of the Mersa Matruh-Shikmona Gyre (MM-S-G) complex are above average. For these deep

[3] This 13.2% rise is partly due to the 4.8% increase in normalized 3D tracer variance explained (from 67.2% at $p = 322$ to 72% at $p = 400$).

[4] To link ratios of standard deviations to ratios of variances, one can use: $(x_2^2 - x_1^2)/2x_2^2 \leq (x_2 - x_1)/x_2 \leq (x_2^2 - x_1^2)/2x_1^2$ with $x_2 > x_1 > 0$.

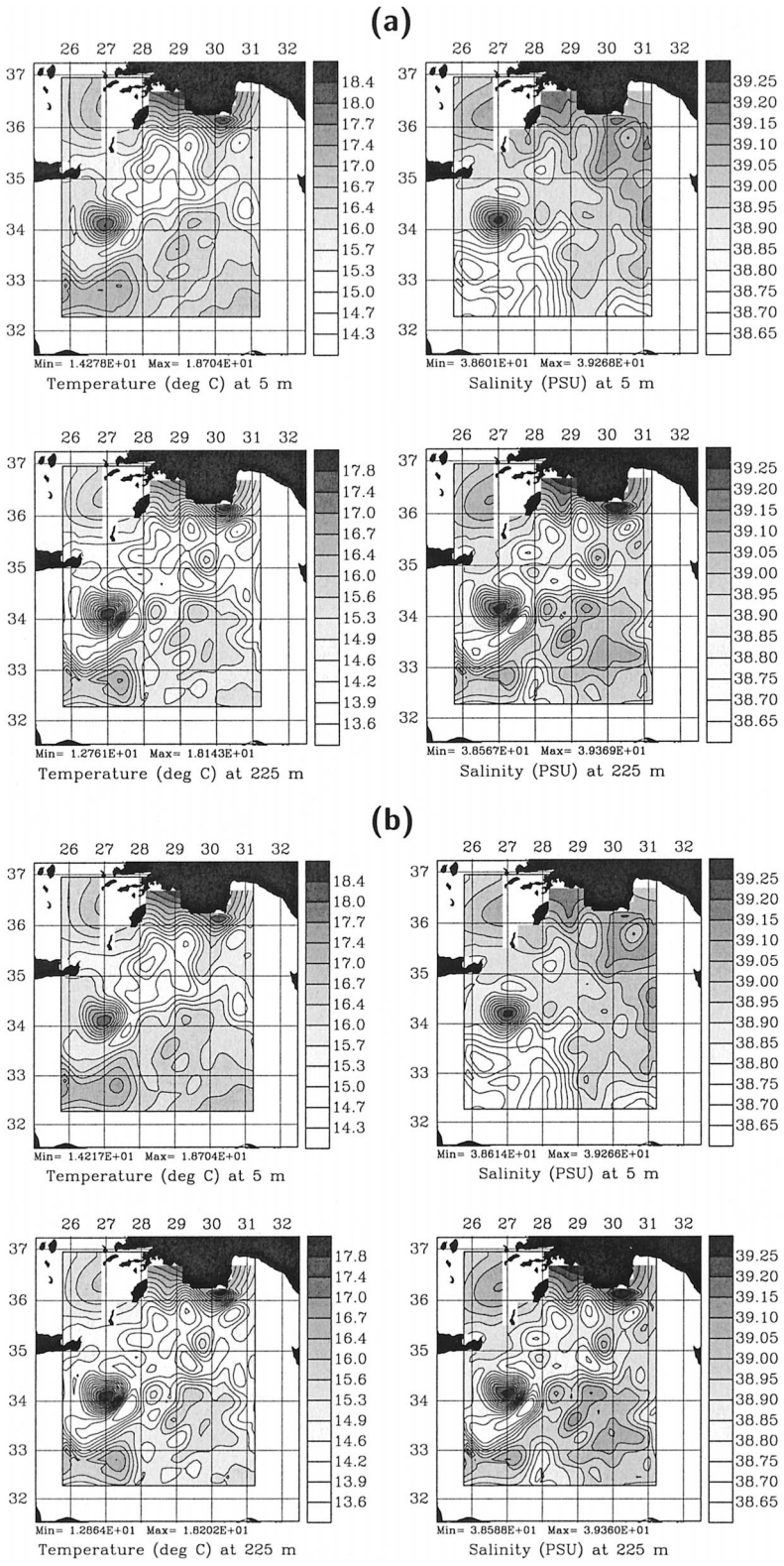

FIG. 8. (a) Total (subbasin-scale plus mesoscale) T and S fields at 5 and 225 m, as estimated by a multivariate 3D error subspace analysis ($w = 2$). The a priori estimate $\mathbf{x}^b_{\text{trc}}$ was illustrated on Fig. 5a. The dominant 500 vectors of $\mathbf{B}_{\text{trc}}$ are used [Eq. (A16)]. Scalings are as on Fig. 6. (b) As (a) but with the dominant 750 vectors of $\mathbf{B}_{\text{trc}}$.

TABLE 1. The four analyses selected and their main differences.

Case	Scheme employed	Size of a priori error subspace	Velocity covariances	Velocity dynamics utilized
1:	Univariate 2D (benchmark)	Full covariances (all 2D vectors)	Not built: direct integration of thermal wind equations	Geostrophy
2:	Multivariate 3D	$p = 322$	Built via an ensemble of adjustment PE integrations	Linear momentum PE model
3:	Multivariate 3D	$p = 322$	As above	Nonlinear momentum PE model
4:	Multivariate 3D	$p = 400$	As above	Nonlinear momentum PE model

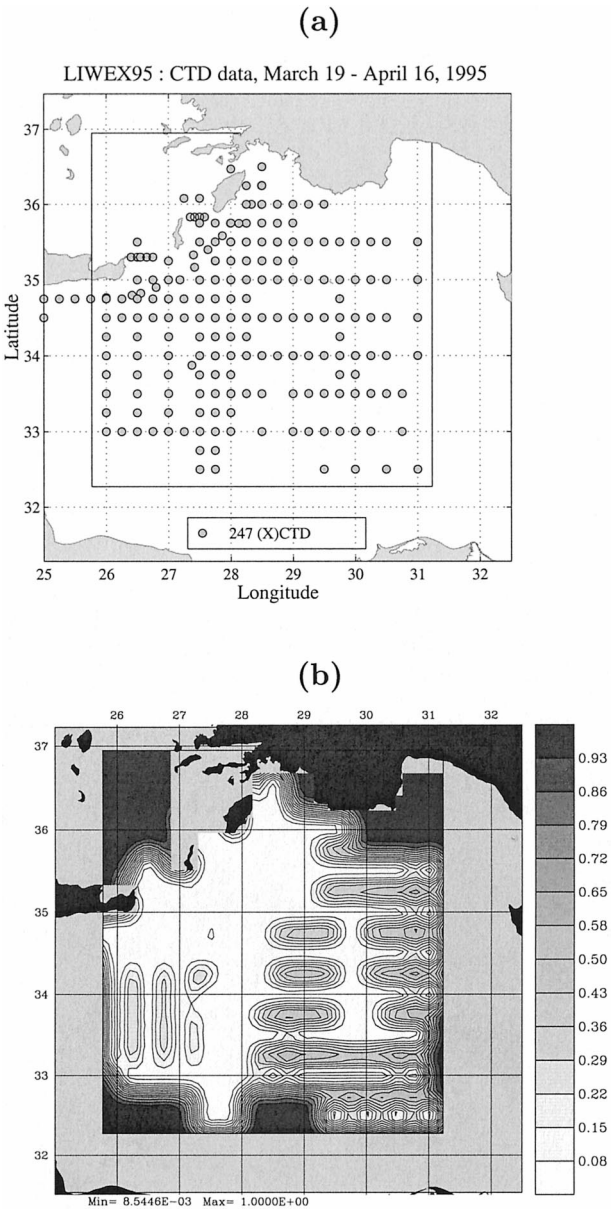

FIG. 9. (a) Coordinates of the 247 CTD profiles gathered during 19 Mar–16 Apr, 236 of which are in the domain and form $\mathbf{y}^o$ (appendix A) in the mesoscale mappings. (b) As in Fig. 2b, surface (5 m) normalized a posteriori mesoscale error variance, but for the data of Fig. 9a.

mesoscale vortices, nonlinear terms matter at depth. In case 4 (nonlinear momentum, $p = 400$), results are as those of case 3, except that standard deviations are a bit larger, to first order by about 6.6%–7.6% (13.2/2–13.2/2/0.868, see footnote 4).

Two general remarks can be made: (i) for accurate flow variability variances, not only the background density field, but also the regional topography, nonlinear, and diffusion terms should be considered; (ii) even though subspaces are used, the present global estimates of mesoscale variances are in accord with and complement previous local estimates (e.g., Özsoy et al. 1993; Robinson and Golnaraghi 1993).

2) A PRIORI MESOSCALE ERROR EIGENVECTORS AND SPECTRUM

Case 2: Figure 10 illustrates the first and second nondimensional singular vectors, columns of $\mathbf{E}^*$ in Eqs. (A21)–(A23). They explain 1.08% and 1.05% of the variance explained by all 322 vectors, respectively. They are examined because several of their properties are representative of those of other dominant vectors. As expected from section 4b(1), for linear momentum, the variability in early spring is dominated by large-mesoscale variations of the Rhodes Gyre. In the last decades, the Rhodes Gyre has indeed been observed to be the main subbasin-scale feature of the region (Milliff and Robinson 1992; Nittis and Lascaratos 1998).

The first vector (Figs. 10, 1a–b) covers the principal core of the Gyre, above the Rhodes Basin. Horizontally (Fig. 10, 1a), the main T and S structures are almost axisymmetric, with horizontal decay scales of about 40 km (radius of 60 km). On the open-ocean side, the main T, S, and ψ structures indicate a predominant geostrophic equilibrium. Close to the coastline, this is not true mainly due to decreasing depth and increasing coastal friction. Vertically, T is surface intensified (Fig. 10, 1b), with a uniform extremum within 20–200 m and a significant extension down to 900–1000 m above the Rhodes Basin. The S structure has a subsurface extremum within 250 to 320 m and a zero crossing near 100 m. The signs of T and S reverse at about 1500 and 1300 m, respectively. Below, local extrema are much smaller than the global upper-thermocline extrema. Overall, where T and S are both relatively large, they are in phase,

TABLE 2. Convergence of and similarity between error subspaces.

a. Convergence coefficient			
For case 2	$\rho_{254-288} = 0.919$	$\rho_{288-322} = 0.930$	
For case 3	Same values as for case 4		
For case 4	$\rho_{288-322} = 0.928$	$\rho_{322-360} = 0.929$	$\rho_{360-400} = 0.935$
b. Similarity coefficient			
Between cases 2–3	$\rho = 0.973$		
Between cases 2–4	$\rho = 0.845$		
Between cases 3–4	$\rho = 0.868$		

compensating each other in density. The surface $\hat{u}$ (Fig. 10, 1a) and cross sections in $\hat{u}$ and $\hat{v}$ (Fig. 10, 1b) confirm a predominant geostrophic equilibrium. A weak topographic wave pattern is also visible in the $\hat{u}$ map and subsurface tracer cross sections. Its average amplitudes are about 20% of those of the main lobes. Vertically, $\hat{u}$ and $\hat{v}$ reverse sign near 700 m. The extrema below are 10 times smaller than the surface ones. Using ψ (Fig. 10, 1a), a minimum total velocity is expected near 900 m.

The second vector (Fig. 10, 2a–b) mainly relates to displacements of the core of the Gyre, along the north–south axis of the Rhodes Basin. Except for the main double lobes in T, S and ψ, and corresponding triple lobes in $\hat{u}$ and $\hat{v}$, most properties are as those of the first vector. Nonetheless, such a displacement of the Gyre's core is logically suggested to interact more with topographic wave patterns (e.g., Smith 1983) than in the first vector. Along the northern escarpment, the dominant wavelength of the pattern (Fig. 10, 2a–b) is about 160 km (scale of 25 km). Possible wave types and timescales are discussed below.

Other dominant vectors also relate to main features (Fig. 1 and Table 3). This is because to explain a natural variation, a group of vectors is usually required. Considering, for example, vectors 3–16, their largest amplitudes assign the vectors: (3–7, 9, 12–16) to the Rhodes Gyre; (3–6, 13–14) to wave patterns along the northern escarpment and Mid-Mediterranean Ridge; (5–9, 11–16) to the Ierapetra; (12–14) to the Mersa Matruh Gyre; (8–16) to the Mid-Mediterranean Jet; (3–4, 6, 9–16) to the West Cyprus Gyre; (4, 6, 9, 12–16) to the Asia Minor Current; and (9–10, 12–16) to the Mersa Matruh-Shikmona Gyre complex. Since each vector is orthogonal to all more dominant ones and 3D dynamical couplings can be complex, a detailed analysis requires additional computations beyond the present scope. Considering the decay of the error spectrum, the variance is distributed such that the dominant 50, 100, and 200 vectors explain 41.4%, 66.7%, and 89.4% of the total variance, respectively.

Case 3: Figure 11 is as Fig. 10, but for nonlinear momentum adjustments (Table 1). In accord with variance results (Table 3), the feature of dominant mesoscale variability is then the Ierapetra. The two vectors shown explain 1.59% and 1.24% of the variance ex-

TABLE 3. A priori mesoscale error std dev for velocity: estimates of cases 2 and 3/4.

Case	Depth	Features (and horizontal averages)	ψ error std dev	Internal velocity error std dev
2	Surface (5 m)	Above the Rhodes Basin	0.85 Sv*	15.5 cm s^{-1}
		Ierapetra	0.8 Sv	14.5 cm s^{-1}
		Mersa Matruh Gyre	0.8 Sv	13 cm s^{-1}
		Mid-Mediterranean Jet	0.68 Sv	13.5 cm s^{-1}
		Surface average	0.65 Sv	12.5 cm s^{-1}
	500 m	Kasos and Karpathos Straits		1.7 cm s^{-1}
		Above the Rhodes Basin		1.3 cm s^{-1}
		500-m average		0.65 cm s^{-1}
3/4	Surface (5 m)	Ierapetra	0.87/0.9 Sv	22/23 cm s^{-1}
		Above the Rhodes Basin	0.87/0.9 Sv	16/16 cm s^{-1}
		Mersa Matruh Gyre	0.84/0.86 Sv	17/18 cm s^{-1}
		Mid-Mediterranean Jet	0.69/0.72 Sv	14/15 cm s^{-1}
		Surface average	0.67/0.7 Sv	13.5/14 cm s^{-1}
	500 m	Kasos and Karpathos Straits		1.75/1.8 cm s^{-1}
		Above the Rhodes Basin		1.4/1.5 cm s^{-1}
		Ierapetra		0.95/1 cm s^{-1}
		Anticyclone in MM-S-G complex		1/1.05 cm s^{-1}
		500-m average		0.68/0.7 cm s^{-1}

* 1 Sv $\equiv 10^6\ m^3\ s^{-1}$.

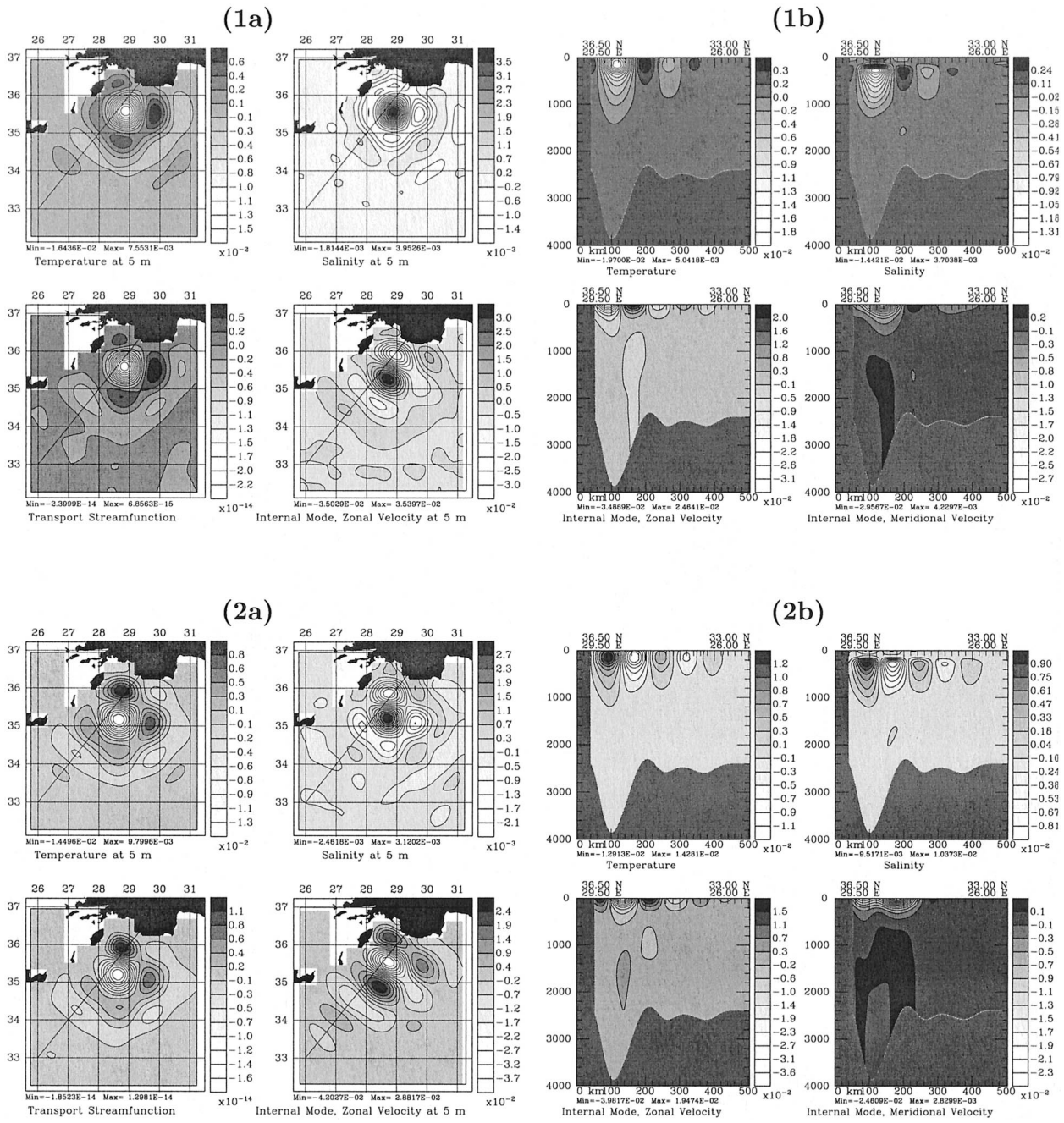

FIG. 10. First two multivariate eigenvectors of the normalized a priori mesoscale error covariance, as estimated by case 2 (Table 1). The panel number is the vector number, with index (a) for the surface (5 m) level, and (b) for a vertical cross section parallel to the Cretan Arc, above the Cretan–Rhodes Ridge [section position drawn in (a)]. The estimation is based on appendix A section b. All variables are nondimensional.

plained by all 322 vectors, respectively. These percentages are larger than in case 2 because nonlinear terms steepen the start and flatten the upper middle of the eigenvalue spectrum. The first vector corresponds to the vortex itself, the second to eastward–westward displacements.

In comparison with case 2, horizontal T and S structures in the first vector (Fig. 11, 1a) are, when significant,[5] closer to Mexican hats and of lesser width (radius

[5] The lobes far from the vortex in surface S are mainly due to the truncation and have an insignificant extremum based on $\rho = 0.928$ (Table 2a). They are excited by radiating nonlinear effects (absent in

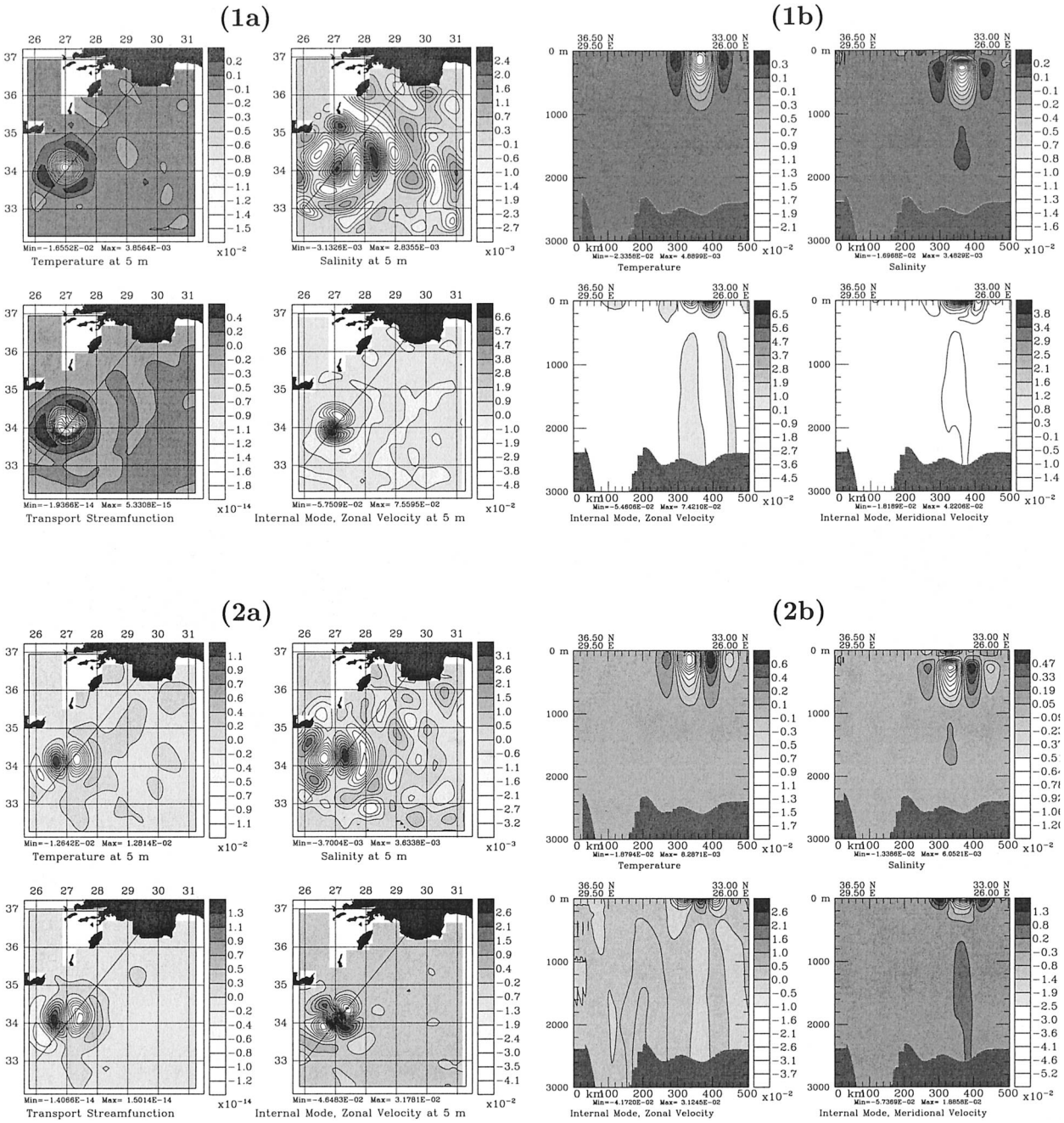

FIG. 11. Same as Fig. 10 but for case 3 (Table 1) and with a different depth range in the cross sections.

near 50 km, decay scale of 30 km). Vertically (Fig. 11, 1b), T and S are more stretched than in case 2, as one expects for a ringlike vortex. Even though T remains surface intensified, its uniform extremum is deeper, within 50 to 250 m. This agrees with previous results: for example, the structure of Levantine warm core eddies (Brenner 1993) and shallow surface mixed layer of the Rhodes Gyre (e.g., Malanotte-Rizzoli et al. 1996). The dominant feature in T extends down to about 600 m, main depth of the present Ierapetra, instead of about 1000 m for the Rhodes Gyre (Fig. 10). The S structure has a zero crossing near 80 m and a subsurface extremum within 250–340 m. The signs in T/S reverse at about 1300 m/1100 m, which, as for the small extrema below, is shallower than at the Rhodes Gyre. Overall, T and S are still in phase when both important. The ψ,

case 2, Fig. 10) and can be seen where amplitudes are relatively small.

$\hat{u}$, and $\hat{v}$ components (Fig. 11, 1a–b) are less close to geostrophic equilibrium than in Fig. 10. The nonlinear, inertial, and viscous terms modify the classic geostrophic antisymmetries of $\hat{u}$ and $\hat{v}$ with respect to the x and y axes. The horizontal lobes (Fig. 11, 1a) present sharp gradients and are tilted, with their heads wider than their tails. Velocity is maximum near a radius of 30 km. Vertically (Fig. 11, 1b), $\hat{u}$ and $\hat{v}$ reverse sign near 400 m, indicating a minimum total velocity near 600 m based on ψ (Fig. 11, 1a). The $\hat{u}$ and $\hat{v}$ extrema below are about 10% of the surface ones. The variations of the deep counterflow and corresponding density are thus weak. However, they have a large vertical extent (here 1500 m) and can influence the stability of the Ierapetra, as found by forecast sensitivity studies in LER97 and argued in general by Dewar and Killworth (1995) and Killworth et al. (1997).

Based on the second vector (Fig. 11, 2a,b), displacements of the Ierapetra can excite radiative momentum patterns. Such adjustments correlate most to density variations in thermal wind balance: note the T and S radiation patterns and horizontal $\hat{u}$ close to a ''45 degree shamrock.'' However, at all depths, $\hat{u}$ and $\hat{v}$ have clear asymmetries and amplitude variations that result from local peculiarities of topography, density, nonlinearities, and bottom friction [section 4b(3)]. In the vertical, most properties are as those of the first vector.

Since the two dominant vectors are modified, the others also differ, even though most of subspace itself remains unchanged (Table 2b). Considering again vectors 3–16, their largest amplitudes assign the vectors: (3–6, 8, 14–16) to the Ierapetra; (6–16) to the Rhodes Gyre; (4, 5, 8) to wave patterns along the northern escarpment and Mid-Mediterranean Ridge; (3–4, 7–10, 12) to the Mersa Matruh Gyre; (8–12, 14–16) to the Mid-Mediterranean Jet; (10–14, 16) to the West Cyprus Gyre; (10, 12, 16) to the Asia Minor Current; and (8–16) to the Mersa Matruh-Shikmona Gyre complex. Overall, the dominant 50, 100, and 200 vectors explain 41.1%, 66.2%, and 89.4% of the total variance, respectively. These percentages are close to those of case 2: the result is that here nonlinear terms impact the dominant vectors of the subspace but do not change much of the overall spectrum.

Case 4: The error subspaces of cases 3 and 4 were estimated to be similar at 86.8% (Table 2b). Up to an arbitrary sign, their vectors 1–15 are almost identical (vectors of case 4 are only slightly less noisy). Some differences start to occur by vector 16, mainly in the small mesoscales. The additional vectors 323–400 include 3D patterns of relatively large horizontal scales and usually ''wiggly'' vertical structures, or vice versa. The decay of the error spectrum is similar to that of case 3: the 50, 100, and 200 dominant vectors explain 38.4%, 62.7%, and 85.2% of the variance explained by all 400 vectors, respectively.

3) Dynamical properties

From the dominant mesoscale vectors and fields obtained, the types and scales of possible wave patterns along the northern escarpment and Mid-Mediterranean Ridge (e.g., case 2), and the dynamical balance of the Ierapetra (e.g., cases 3–4) can be investigated. Note that the numbers obtained from cases 3 and 4 are similar, indicating a robustness of the results.

Wave patterns: Using app. B and Fig. 10, locally for a wave packet along the escarpment, $\rho_0 = 1028$ kg m^{-3}, $L = 25$ km, D is about 1000 m, H is on Fig. 2c, $f_0 = 8.45\ 10^{-5}$ s^{-1}, and $\beta_0 = 1.86\ 10^{-11}$ m^{-1} s^{-1} (for $\theta_0 = 35.5°$). Computing a reference $\rho_s(z)$ by horizontal average of the density field, this leads an average N_s within D of about $2.5\ 10^{-3}$ s^{-1}, a local $R_D = N_s D/f_0 \simeq 30$ km, and $R_{\text{ext}} \simeq 1200$ km. For U, based on the second vector (Fig. 10, panels 2a, b), the sum of the surface internal and external components yields: $U \simeq (3.9 \times 1.5\ 10^{-2} + 5.6\ 10^{7} \times 0.5\ 10^{-2}/H/L)\ (1893)^{1/2} \simeq 3$ cm s^{-1} ($1.5\ 10^{-2}$ and $0.5\ 10^{-2}$ are the nondimensional amplitudes, 3.9 and $5.6\ 10^{7}$ the normalization factors, and 1893 the eigenvalue). With contributions from other relevant vectors, the characteristic velocity U for a wave packet is about 5 cm s^{-1}. Hence, the local nondimensional numbers are $Ro = 0.015$, $Bu_{\text{ext}} = 2\ 10^{3}$, $Bu = 1.4$, $\beta = 0.23$, $\alpha \simeq 25$, and $s \simeq 0.6$ (except just east of the island of Rhodes where α and s reach 50 and 1, respectively). The small Ro and large Bu_{ext} indicate that the rigid-lid linear PE regime is appropriate. From β, the planetary vorticity gradient is relatively small and from $\alpha \gg 1$, the topographic vorticity gradient is large: β_0 can be neglected compared to $|\nabla_h H| f_0/D$. From $Bu \sim 1$, the length scales of the horizontal flow and internal stretching (stratification's strength) match. Since s is close to one, quasigeostrophy may not apply. Finally, for the model topography (Fig. 2c), s and α are relatively uniform along the escarpment waveguide (about 60 km wide). Based on these numbers and interpretations, the topographic wave packets are of the coastal-trapped type (Huthnance 1992; Pedlosky 1987; Brink 1991). Note that here, wave patterns arise during rigid-lid momentum adjustments (fixed tracer disturbances): for the barotropic mode along the escarpment, to first-order in s, the frequency is then of the order $(|\nabla_h H| f_0/D)/k$, where $k = 1/L$ is the wavenumber. This leads a period of about 1.45 days, that is, of the order of 1 to 2 days.

In the ocean, wave packets would be generated by complete dynamical adjustments, and also by winds, atmospheric pressure, and coastal flows. A complex wave spectrum around the above values can be expected. First, the natural topography is more jagged and at several locations steeper than the model topography, which we estimate could shift the period by about 50%. Second, several wave types are possible along the escarpment and/or Mid-Mediterranean Ridge: in addition to a suite of coastal-trapped waves (e.g., Leblond and Mysak 1971) like Kelvin and continental shelf waves,

inertial and Rossby waves can be generated. For complete statements on scales, shapes, and forcings, additional studies are necessary (e.g., Huthnance 1978; Holland and Webster 1994). The dominance of such wave patterns and associated mesoscale variations in the vectors related to the Rhodes Gyre [section 4b(2)] suggests that they could be in part responsible for the observed multiple centers of the Gyre (Milliff and Robinson 1992). In particular, the main core of the Gyre is not stationary, but undergoes translations and precessions of synoptic timescales (seen in our simulations).

Ierapetra: Using Fig. 11 and local scale analysis, an approximate dynamical balance for the Ierapetra can be obtained. One has $\rho_0 = 1028$ kg m^{-3}, $L = 20$ km, $D = 400$ m, $H \simeq 2500$ m (Fig. 2c), $f_0 = 8.15\ 10^{-5}$ s^{-1}, and $\beta_0 = 1.89\ 10^{-11}$ m^{-1} s^{-1} (for $\theta_0 = 34.1°$). The vertical averages within D of N_s and of the horizontal $\Delta\rho$ are $2.5\ 10^{-3}$ s^{-1} and 0.15 kg m^{-3}, respectively. Hence, $R_D = 12$ km and $R_{\text{ext}} = 770$ km. From Table 3, the mesoscale component of the total surface U is 25 cm s^{-1}. Adding the subbasin-scale component (section 4a) yields $U \simeq 45$ cm s^{-1}. Hence, for the Ierapetra, relevant nondimensional numbers are $Ro = 0.28$, $Bu_{\text{ext}} = 1500$, $Bu = 0.38$, $\beta = 0.017$, $\alpha = 1.8$, and $s = 0.5$. The size of Ro attests that nonlinearities are important while β and Bu_{ext} confirm that the planetary vorticity and stretching of the free surface do not matter. The above numbers suggest that the dominant horizontal momentum balance within the vertical extent D is the gradient–wind balance: solving for U in $U^2/L - f_0 U + \Delta\rho g D/\rho_0 L \simeq 0$ gives a root $U \simeq 50$ cm s^{-1} (accounting for the uncertainty in characteristic scales, this root lies between 40 and 70 cm s^{-1}). In the vertical, since Ro and Bu are of the same order, W is large enough for the vertical convergence and horizontal divergence to balance ($W \simeq UD/L$) and the horizontal changes in density to match the vertical ones ($\Delta\rho \simeq \Delta\rho_s$). Based on α and s, the local topographic valley (Fig. 2c) is a factor in maintaining the location of the vortex. Finally, viscous terms are only important in the bottom layers and at the submesoscales: for examples, the horizontal momentum Ekman number $Ek_h = A_h/f_0 L^2$ is 0.92 for scales under 20 km but decays to $5\ 10^{-4}$ at 50 km and is almost null beyond 100 km (A_h is the effective Laplacian horizontal eddy viscosity, which is here scale dependent).

4) A PRIORI MESOSCALE ERROR COVARIANCE FUNCTIONS

The covariance function between the surface (5 m) temperature at (33.80°N, 27.85°E: about 80 km east-southeast of the Ierapetra) and the other state variables is chosen as an example. The plots (Figs. 12–13) correspond to elements of a row of $\mathbf{B}^p$ (size 218943 × p).

Case 2: Figure 12 shows that the horizontal T–T and T–S Mexican hat covariances are well represented. Vertically (Fig. 12b), the characteristics of tracer covariances are T–T and T–S uniform within a 30-m surface mixed layer; subsurface extremum in T–S near 300 m; T–T and T–S positive down to about 1200 m where they change sign; etc. For T–ψ (Fig. 12a), quasigeostrophic balance is locally a good approximation. However, the horizontal T–$\hat{u}$ and T–$\hat{v}$ are not exactly antisymmetric, geostrophic double-lobe structures. At the surface, the main reason is that inertial terms matter at (33.80°N, 27.85°E). If only the inertial and geostrophic terms were important, after 2 days of adjustment integration, with $2\pi/f \simeq 0.89$ days, the T–$\hat{u}$ pattern at 5 m would be tilted clockwise by almost 45°. With horizontal, vertical and bottom diffusion, this tilt at 5 m is here reduced to about 30° (Fig. 12a). Note that even though inertial oscillations occur (e.g., in numerical simulations, the Ierapetra at the surface rotates in small circles at frequencies close to f), their effects on covariances are not always desired.[6] In the vertical (Fig. 12b), T–$\hat{u}$ and T–$\hat{v}$ have a zero crossing within 500–600 m. From T–ψ, total velocity covariances near (33.80°N, 27.85°E) have a vertical minimum near 700 m. Below the zero crossings, T–$\hat{u}$ and T–$\hat{v}$ are opposite to their surface structures, but as in section 4b(2), amplitudes are much smaller (at most 10% of surface values).

Cases 3 and 4: By construction, the tracer autocovariance functions of cases 3 and 2 (Fig. 12) are equal. Those of case 4 are very similar; the main difference is a volume-averaged increase in variance of 100 × (72 − 67.2)/67.2 = 7.1% (section 4b), which is distributed in the 3D T–T and T–S fields according to the tracer vectors 323 to 400. Figure 13 thus only illustrates cross-covariances with velocities. Comparing cases 2 (Fig. 12) and 3 (Fig. 13a), overall, nonlinear momentum adjustment modifies structures, but amplitudes remain similar. Focusing on differences, the horizontal T–$\hat{u}$ structure has a smaller tilt, of about 15°–20° clockwise: the nonlinear terms dissipate some inertial oscillations. Cross-covariances now extend to the Ierapetra and their gradients are tighter due to nonlinearities. The T–ψ structure has become asymmetric, with cyclonic T–ψ correlations at the Ierapetra. In the vertical, structures in the upper layers extend deeper. Other vertical changes are mainly due to the lesser 15°–20° rotation in the horizontal. Considering the velocity cross-covariances of cases 3 (Fig. 13a) and 4 (Fig. 13b), shape and amplitude differences are small. This agrees with the corresponding global similarity coefficient (Table 2b).

c. Mesoscale: A posteriori PE fields

At the mesoscale stage ($w = 2$), the mapping procedures are as overviewed in section 4a. The differences

[6] Undesired effects of inertial oscillations arising in adjustments can be made insignificant by allowing the duration of adjustment integrations to be random within an inertial period. This would be useful inside the Rhodes Gyre where nonlinear terms are weak: the tilt in the 5 m T–$\hat{u}$ and T–$\hat{v}$ covariances there mainly depends on the duration of adjustment, due to inertial rotations. However, at the Ierapetra where nonlinear terms dominate, the duration of adjustment did not influence the tilt in velocity covariances (the tilt is desired).

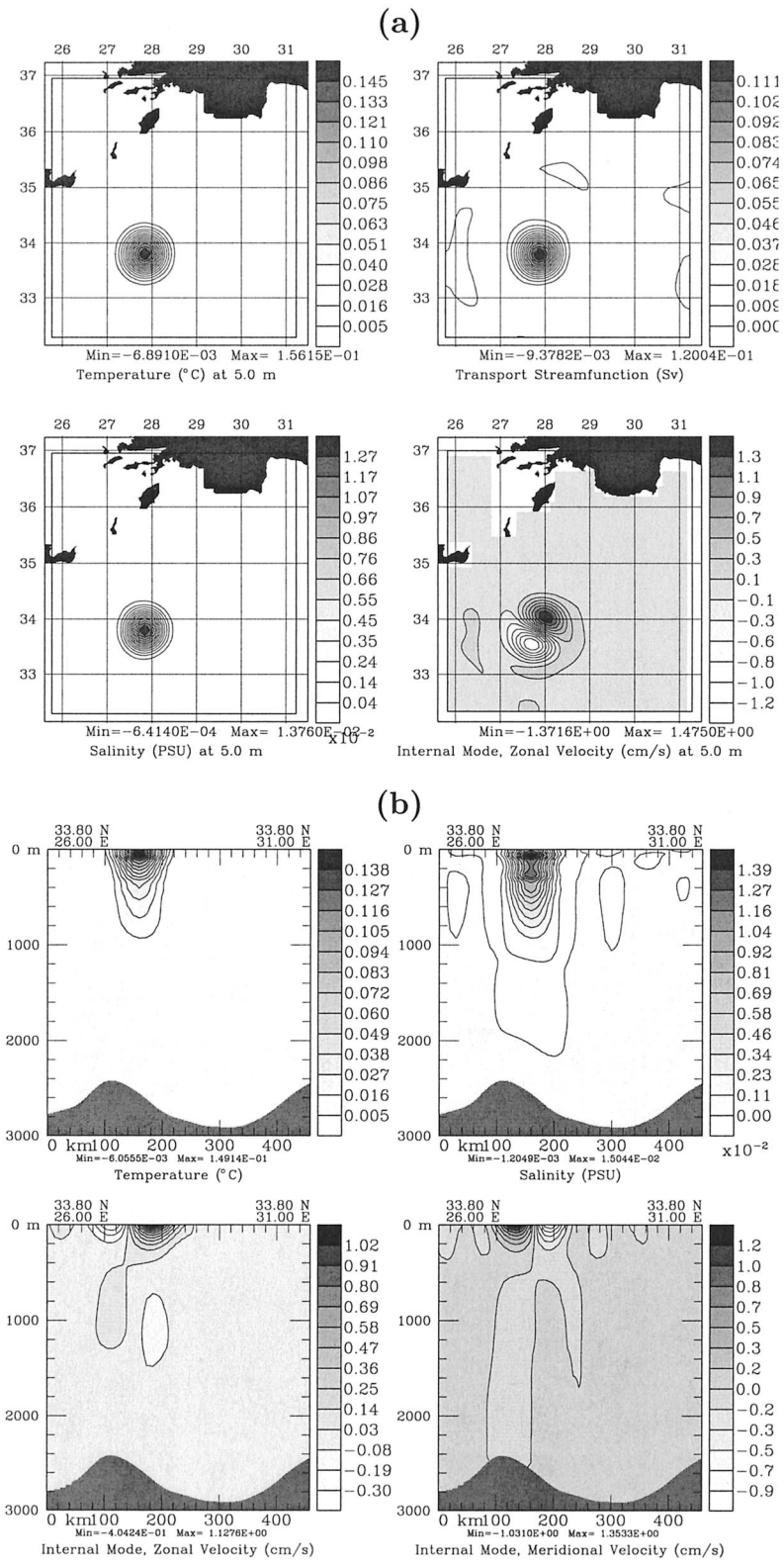

FIG. 12. Case 2 estimate of the dimensional mesoscale covariance functions between the 5-m temperature at (33.80°N, 27.85°E) and the other state variables [only the later are listed in bottom labels, e.g., T (°C) stands for T–T covariance (°C²), S (psu) for T–S covariance (°C psu), etc.]. (a) Values on the first level (5 m); (b) zonal cross sections along 33.80°N.

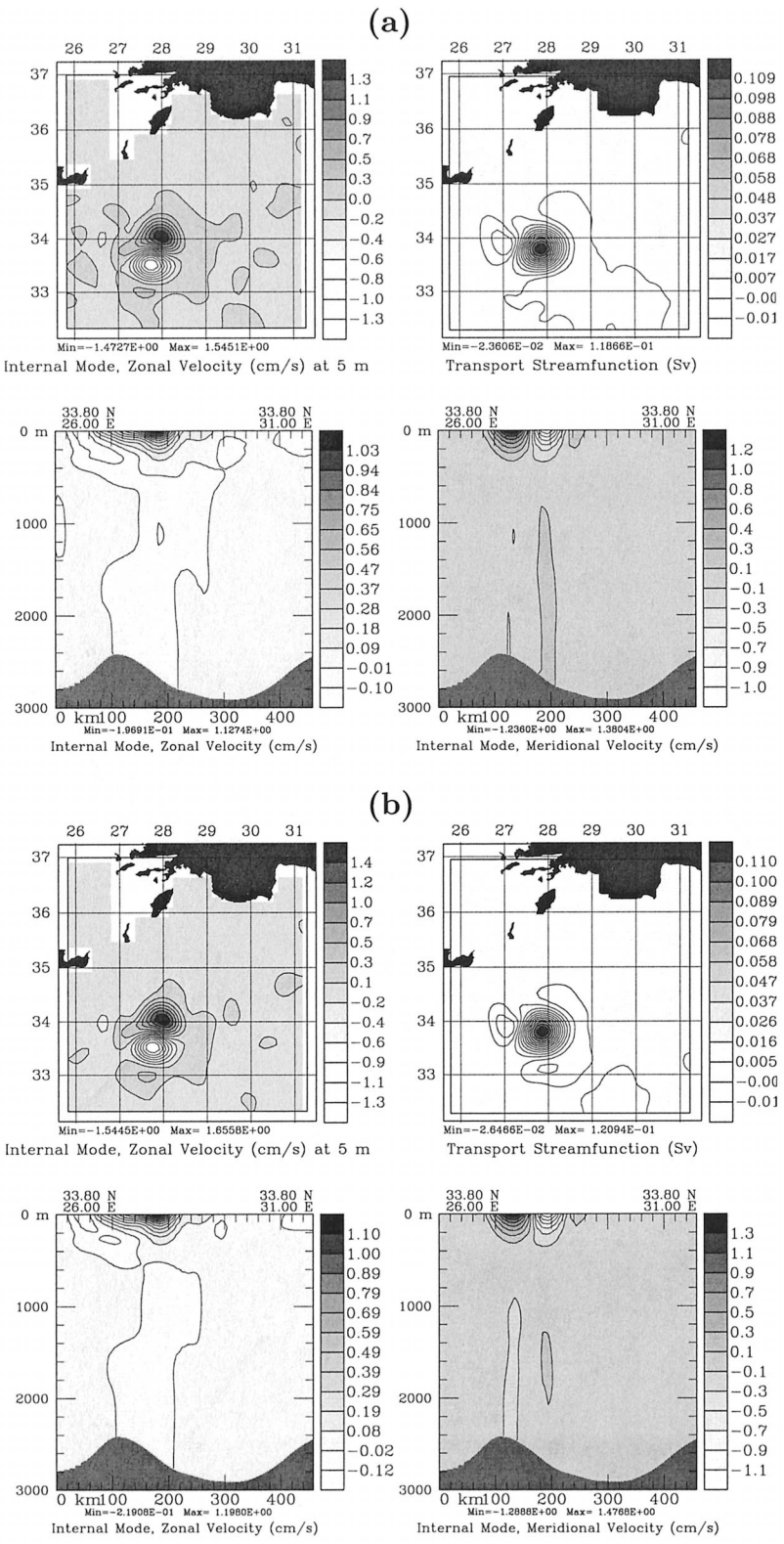

FIG. 13. As in Fig. 12 but (a) for case 3, (b) for case 4, and only plotting temperature–velocity cross-covariance functions. These functions are still shown on the first level (5 m) and in zonal cross sections along 33.80°N.

lie in the a priori states (the subbasin-scale estimates), dataset, and mesoscale covariances (section 4b). The focus next is on cases 2 and 3 for the effects of nonlinear momentum terms, and on cases 3 and 4 for the effects of the size of the subspace.

1) TRACER FIELDS

Figure 14 illustrates the *T, S* components of $\mathbf{x}^a$ obtained by multivariate 3D analysis (appendix A section c) in case 2. By construction, the tracer fields for case 3 (not shown) are identical. Comparing cases 2 (Fig. 14) and 4 (Fig. 10 in LAL00), their tracer fields have small differences, in accord with the 4.8% (67.2%–72%) increase in the 3D tracer variance explained. Differences are largest in the surface layers and small mesoscales, which is the main variability spanned by the additional vectors 323 to 400 used in case 4. In comparison with case 1 (Figs. 9 in LAL00), results are analogous to these of section 3. The large mesoscales to the subbasin-scales have small differences, within data error bounds. The submesoscales to small mesoscales present larger differences, especially near the surface. This is because many of these small scales are environmental noise for the available data resolution (Fig. 9a) and because the 400 eigenvectors explain only 72% of the total tracer variance (section 4b).

2) TRANSPORT FIELDS

Figure 15a is the result of case 1 that computes ψ by vertically averaging the total velocities in thermal wind balance with the horizontal *T* and *S* analyses, assuming a level of no motion at 600 m. Figure 15b is the ψ component of $\mathbf{x}^a$ for case 2: the transport is then globally estimated from the *T* and *S* data (Fig. 9) using appendix A section c. Figure 15c is ψ for case 3, Fig. 15d ψ for case 4. The advantages of cases 2–4 are that their ψ estimates, and corresponding uncertainties (section 4d), are in accord with the dominant SVD of PE adjusted perturbations. Most of the regional dynamical features can be distinguished in these ψ fields, but not in those of case 1. Comparing Figs. 15b and 15c, the effects of nonlinear terms in the momentum adjustments agree with local mesoscale standard deviations (Table 3). Differences are largest for the Ierapetra and Mersa Matruh Gyre. Comparing Figs. 15c and 15d, increasing the size of the subspace leads to small 2% to 10% variations in ψ, in accord with the global covariance similarity of 86.8% (Table 2b). Largest changes are at the Ierapetra, above the Rhodes basin and along the Asia Minor Current and Mid-Mediterranean Jet.

3) INTERNAL VELOCITY FIELDS

Figure 16a is the result of case 1, which computes $\hat{u}$, $\hat{v}$ by thermal wind balance. Figure 16b are the surface $\hat{u}$, $\hat{v}$ components of $\mathbf{x}^a$ for case 2: $\hat{u}$, $\hat{v}$ are then globally estimated from the *T* and *S* data (Fig. 9) using appendix A section c. Figure 16c is the same, but for case 3; Fig. 16d is for case 4. Differences between cases 1 and 2 are small and mainly due to their different tracer fields. Nonlinear momentum terms (cases 2 to 3) mainly affect the Ierapetra and Mersa Matruh Gyre. For the Ierapetra, gradient–wind balance [section 4b(3)] is a good approximation but geostrophy is not. Increasing the size of the subspace (cases 3 to 4) leads to variations in the small mesoscales, in accord with the variability spanned by the additional vectors considered. Overall, the regional increases in speed from cases 2 to 3, and from cases 3 to 4, agree with the a priori standard deviations of Table 3 and global values obtained from Table 2b.

d. Mesoscale: A posteriori error covariance

1) A POSTERIORI MESOSCALE ERROR VARIANCE

Univariate 2D benchmark: A posteriori tracer error variances result from the 2D analyses, for example, 5-m errors on Fig. 9b. Velocity error variances are set assuming geostrophic balance.

Multivariate 3D scheme: Figures 17a–b illustrate a posteriori error standard deviations for cases 2 and 3 (for case 4, see Fig. 13 of LAL00). An important result is that error properties are as one expects dynamically even though only 322 or 400 vectors are used. The tracer errors of cases 2–4 are similar to those of case 1 (Fig. 9b). Differences are due only to the use in cases 2–4 of a priori *T* and *S* covariances with nonzero multivariate and vertical correlations. By construction, tracer errors for cases 2 and 3 are identical (up to machine precision).

In general, the structures of velocity errors (Figs. 17a–b) differ from those of tracer errors, which mimic the patterns of hydrographic ship-tracks. Differences in shape are much larger for $\hat{u}$, $\hat{v}$ errors (under geostrophic influence) than for ψ errors (under hydrostatic influence). The relationships among velocity error patterns, regional dynamical features, and data horizontal and vertical resolutions (unsampled regions, distances between ship-tracks, spacings between profiles along ship-tracks, nonuniform profile lengths, etc.) are discussed in section 5.b.ii of LAL00. These discussions apply here. Focusing on sensitivities, velocity errors for cases 2–4 differ from these of case 1 (not shown) because, in cases 2–4, a priori error covariances involving velocities are nonhomogeneous and anisotropic in 3D and because the dominant momentum balance is not everywhere geostrophy (diffusion and nonlinearities matter locally). Comparing cases 2 (Fig. 17a) and 3 (Fig. 17b), the nonlinear momentum terms impact a posteriori errors in ψ, $\hat{u}$, and $\hat{v}$ at various depths and locations. Differences are largest near the Ierapetra, Mersa Matruh Gyre, and Mersa Matruh-Shikmona Gyre complex, which we found to be the most nonlinear features a priori (section 4b). Due to nonlinear mixing, error patterns in case 3 are broader and more uniform (less de-

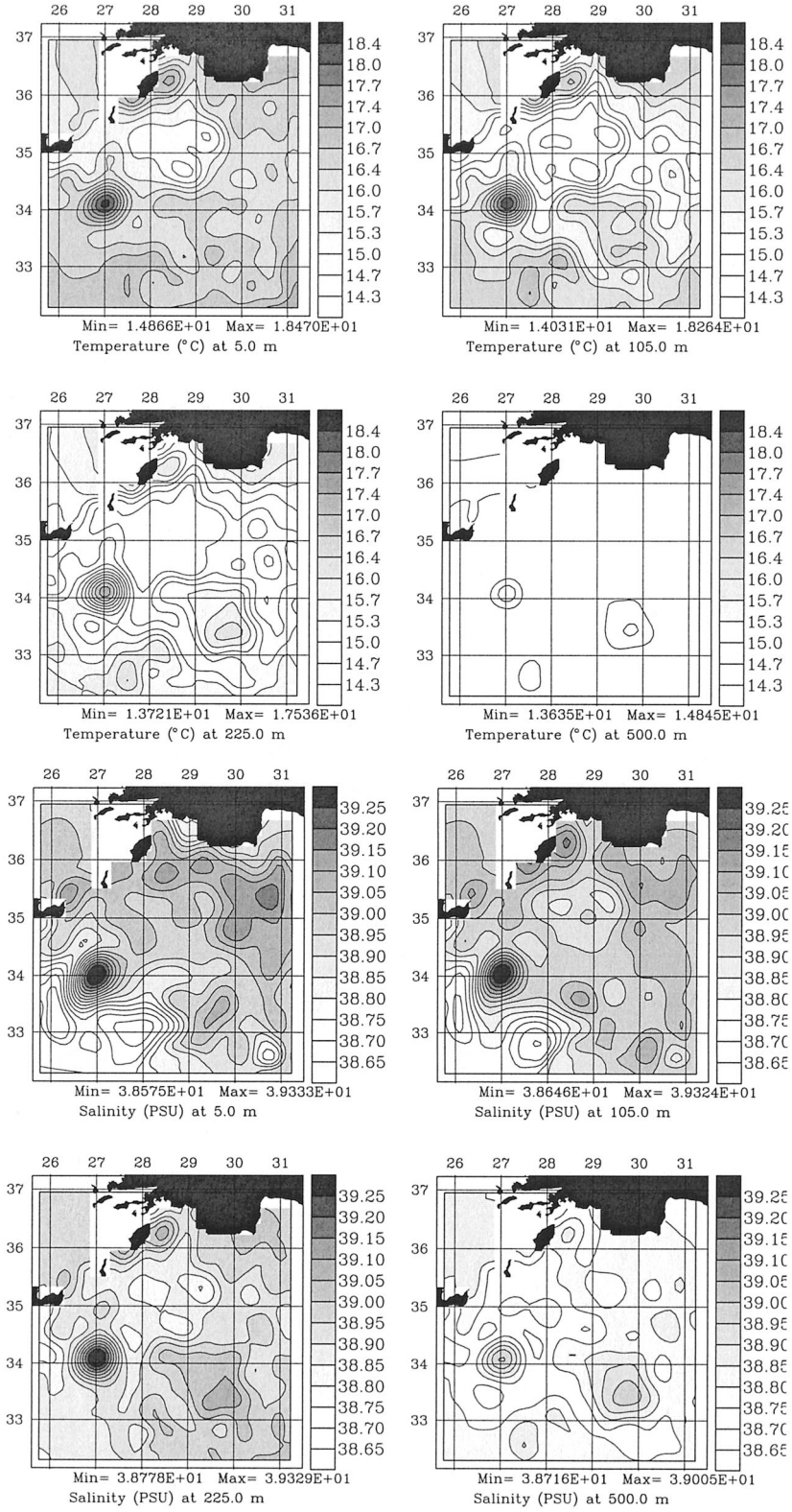

FIG. 14. Case 2: Total (subbasin-scale plus mesoscale) T and S fields resulting from a multivariate 3D analysis. The dominant 322 vectors of $\mathbf{B}^p$ in Eq. (A23) are used. The levels shown and scalings are as in Figs. 9–10 of LAL00. The corresponding first-stage fields resulted from a subbasin-scale multivariate 3D analysis.

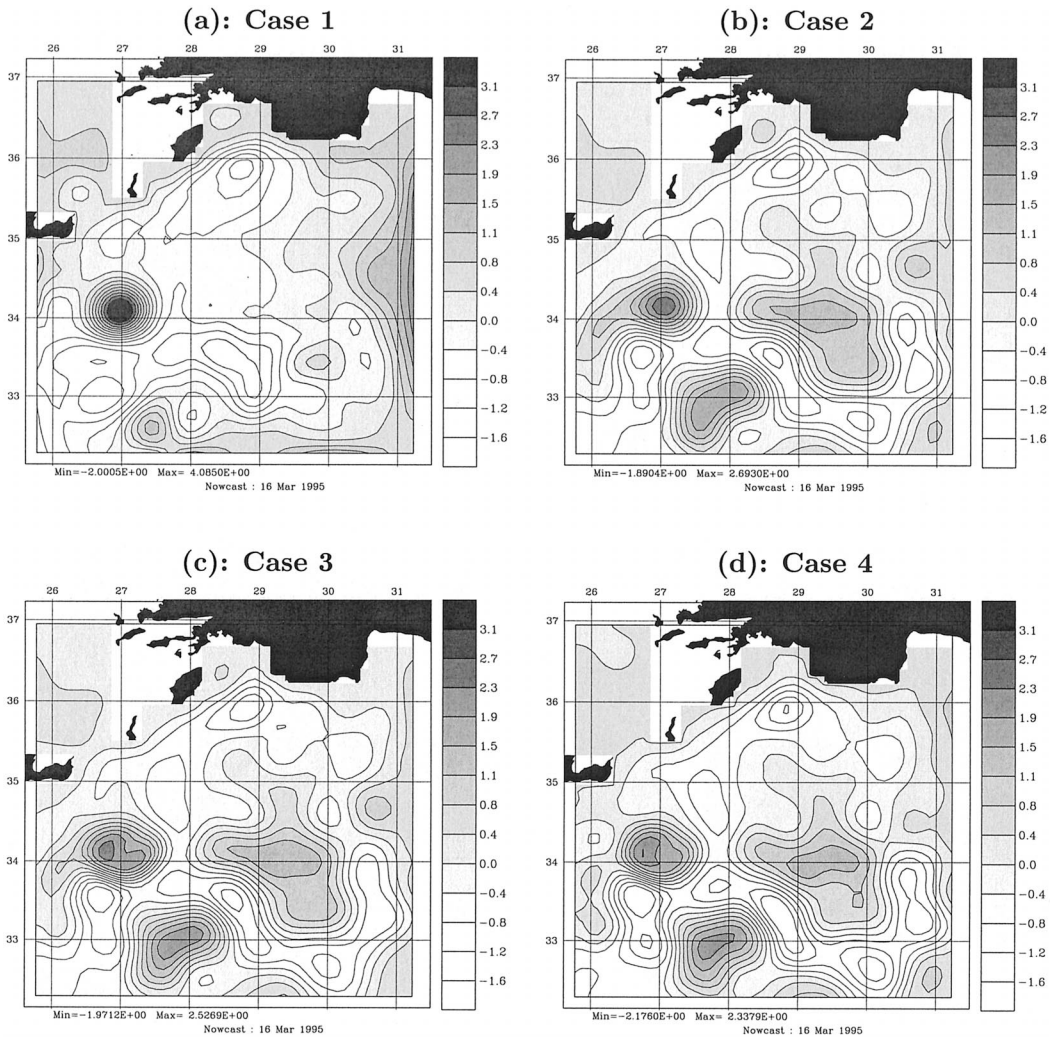

FIG. 15. Total (subbasin-scale plus mesoscale) barotropic transport streamfunction estimates (ψ in Sv; Sv $\equiv 10^6$ m^3 s^{-1}). (a) Univariate 2D scheme. (b) Multivariate 3D analysis, with $p = 322$ and linear momentum adjustment. (c) As (b) but with a nonlinear momentum adjustment. (d) As (c) but with $p = 400$ vectors.

pendent on data location) than in the linear case 2. The local variations at depths (see LLA98) among cases 2–4 are in accord with global dissimilarities (Table 2b) and differences in a priori error fields [section 4b(1)].

2) A POSTERIORI MESOSCALE ERROR EIGENVECTORS AND SPECTRUM

The first and second nondimensional a posteriori error singular vectors for cases 2 and 3 are illustrated on Figs. 18 and 19, respectively (for case 4, see Fig. 14 of LAL00). For each of cases 2–4, the data $\mathbf{y}^o$ have redistributed the variance in the subspace. Dominant a posteriori vectors have little in common with a priori ones. In the linear case 2 (Fig. 18), the two dominant vectors are associated with the low data resolution along 30.75°E (Fig. 9a) and lack of data in the northeast corner (north of 35.5°N, east of 29.5°E). In cases 3 (Fig. 19) and 4, this holds for the first vector, but not for the second. The second vector then corresponds to low data resolution patches centered on 29°E, which is across the Mersa Matruh-Shikmona Gyres where nonlinearities matter (section 4b). In case 2, the first vector accounts for 5.7% of the normalized a posteriori error variance; the second for 5.1%. In case 3, these numbers are smaller, 5.2% and 4.8%, because some additional kinetic energy due to nonlinear terms remains unmeasured in the a posteriori eigenvalue spectrum. In case 4, these numbers further reduce to 4.25% and 4.05% due to the larger subspace size. Overall, eigenvalue spectra differ for the same reasons, but by smaller amplitudes. In case 2, the dominant 50 vectors explain 75.8% of the variance explained by all 322 vectors; the dominant 100 explain 87.2%. In case 3, these numbers remain nearly unchanged, 75.5% and 87.2%. In case 4, they are logically slightly smaller: 71.5% for 50 vectors and 84.5% for

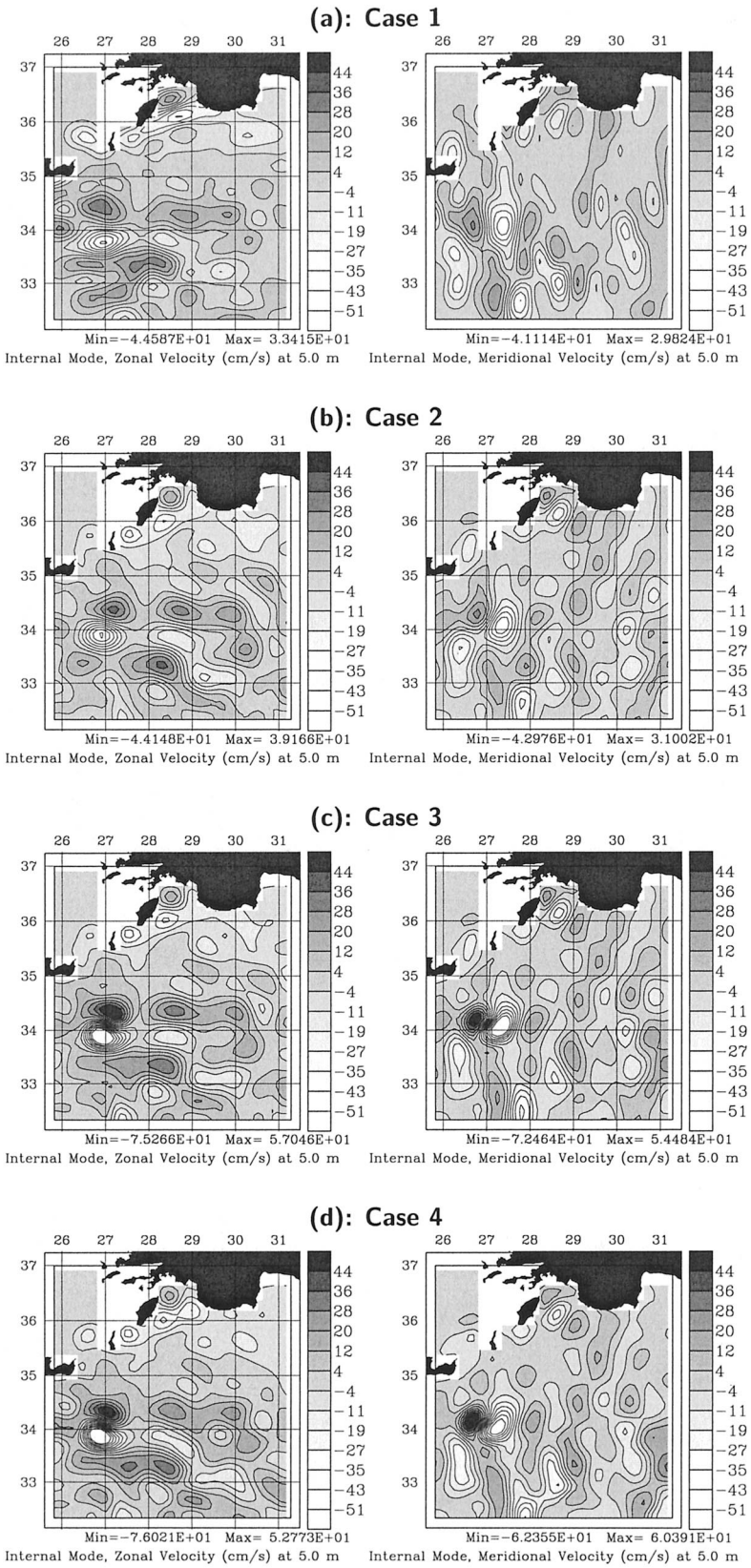

FIG. 16. Total (subbasin-scale plus mesoscale), zero-vertical mean, internal velocity estimates ($\hat{u}$, $\hat{v}$) at 5 m (cases as in Fig. 15).

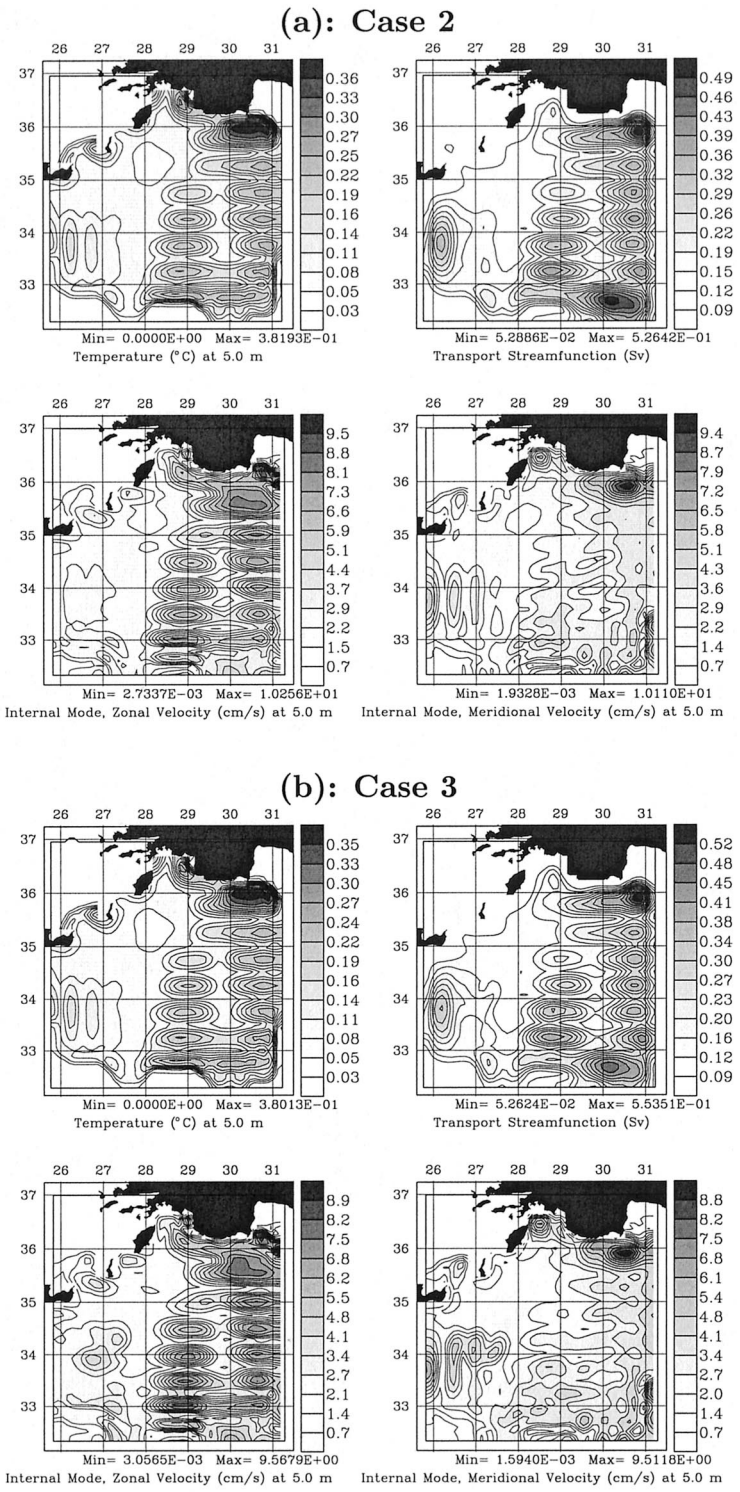

FIG. 17. (a) Multivariate a posteriori error std dev for case 2. The square root of the diagonal of $\mathbf{E}^a\mathbf{\Pi}^a\mathbf{E}^{aT}$ (appendix A section c) is illustrated: the surface (5 m) error std dev of T, $\hat{u}$, and $\hat{v}$, and the ψ error std dev are shown. (b) As (a) but for case 3.

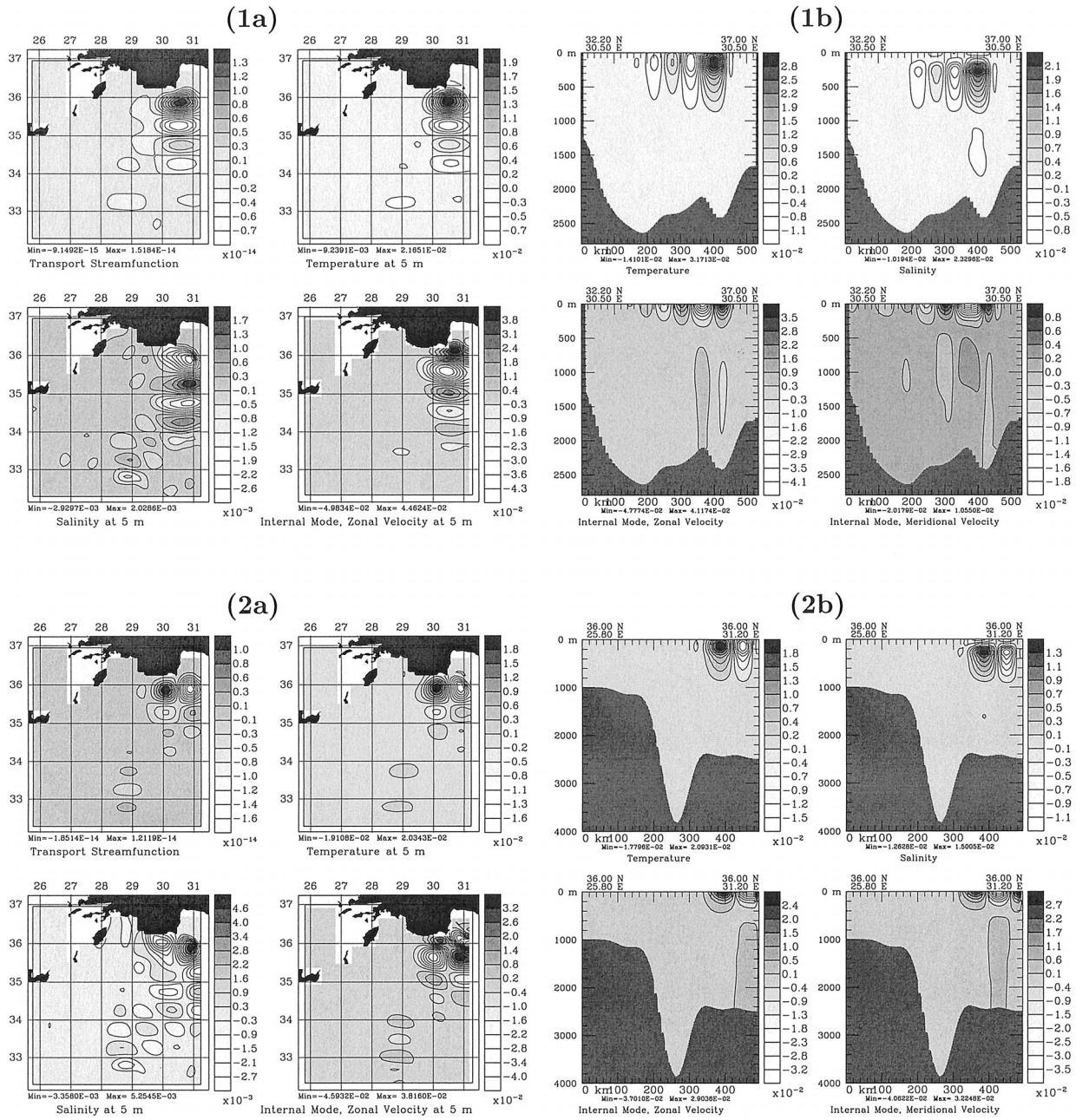

FIG. 18. First two multivariate eigenvectors of the normalized a posteriori mesoscale error covariance (columns of $\mathbf{E}^{a*}$, appendix A section c), as estimated by case 2. The panel number is the vector number, with index (a) for the surface (5 m) level, and (b) for a vertical cross section along an axis of large amplitudes (30.50°E for vector 1, 36°N for vector 2). All variables are nondimensional.

100 vectors out of all 400 vectors. For all cases, in comparison to a priori values [section 4b(2)], the analysis has here steepened the top and flattened the middle and end of the error spectrum.

Structurewise, cases 2–4 have almost the same first vector (Figs. 18–19, panels 1a–b). Due to the nonlinear adjustments, other vectors are reordered in cases 3–4: for example, up to effects of the orthogonality constraint and arbitrary sign, the second vector of case 2 is as the third of case 3 (not shown) and inversely (Fig. 19). However, the dominant vectors of cases 3 and 4 are almost identical, indicating a convergence. Locally, both dynamics and data affect all vectors. Focusing here on data coverage (see LAL00 for dynamical effects), consider, for example, the first vector of cases 2–4 (Figs. 18–19, panels 1a–b). For each variable, amplitudes north of 35.5°N in the corner without data are at least twice as large as they are south of 35.5°N. The zero

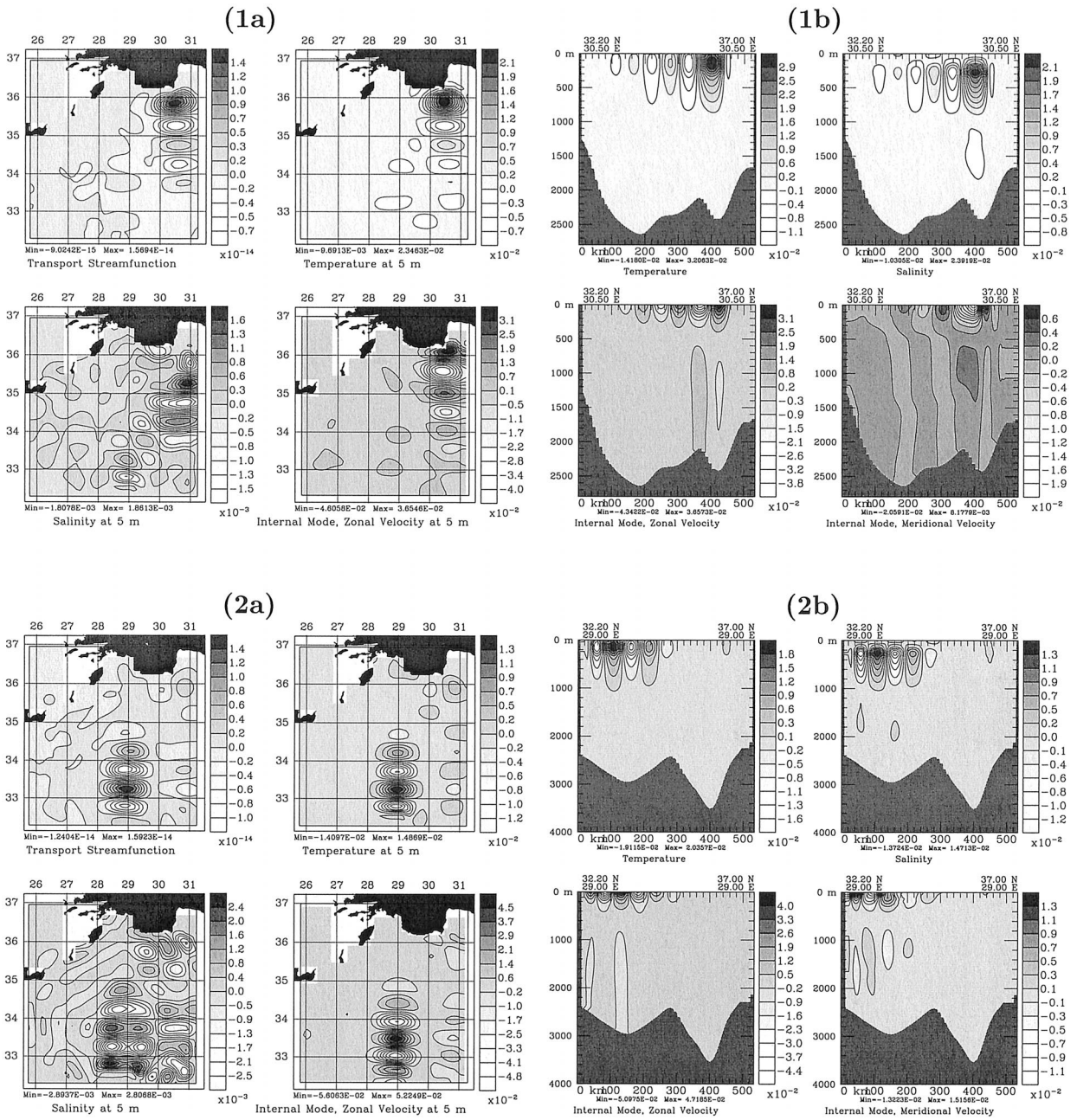

FIG. 19. As Fig. 18 but for case 3: the vertical cross sections are along 30.50°E for vector 1, but along 29°E for vector 2.

crossings (maxima) of the T and S patterns of this first vector are also aligned with the (lack of) meridional ship-transects (Fig. 9): from 34°N to 35.5°N included, zero crossings are every 0.5° latitude, while north of 35.5°N, the last lobe covers 0.8° latitude, across the no-data corner. Profile depths also influence error patterns. For example, east of 30.25°E, all profiles are about 1000 m deep, except for two at (35.5°N, 31°E) and (34.5°N, 31°E), which are 2000 m deep. Logically, these two deep profiles reduce the error on $\hat{u}$ at 35°N but not on $\hat{v}$ [see Figs. 18(1b) and 19(1b) from 1000 to 2000 m]. Analogous facts hold for other vectors.

3) A POSTERIORI MESOSCALE ERROR COVARIANCE FUNCTIONS

Comparing a priori [Figs. 12–13, section 4b(4)] and a posteriori (Figs. 20–21) error covariance functions also shows data impacts. All amplitudes are reduced in accord with the data coverage and measurement error

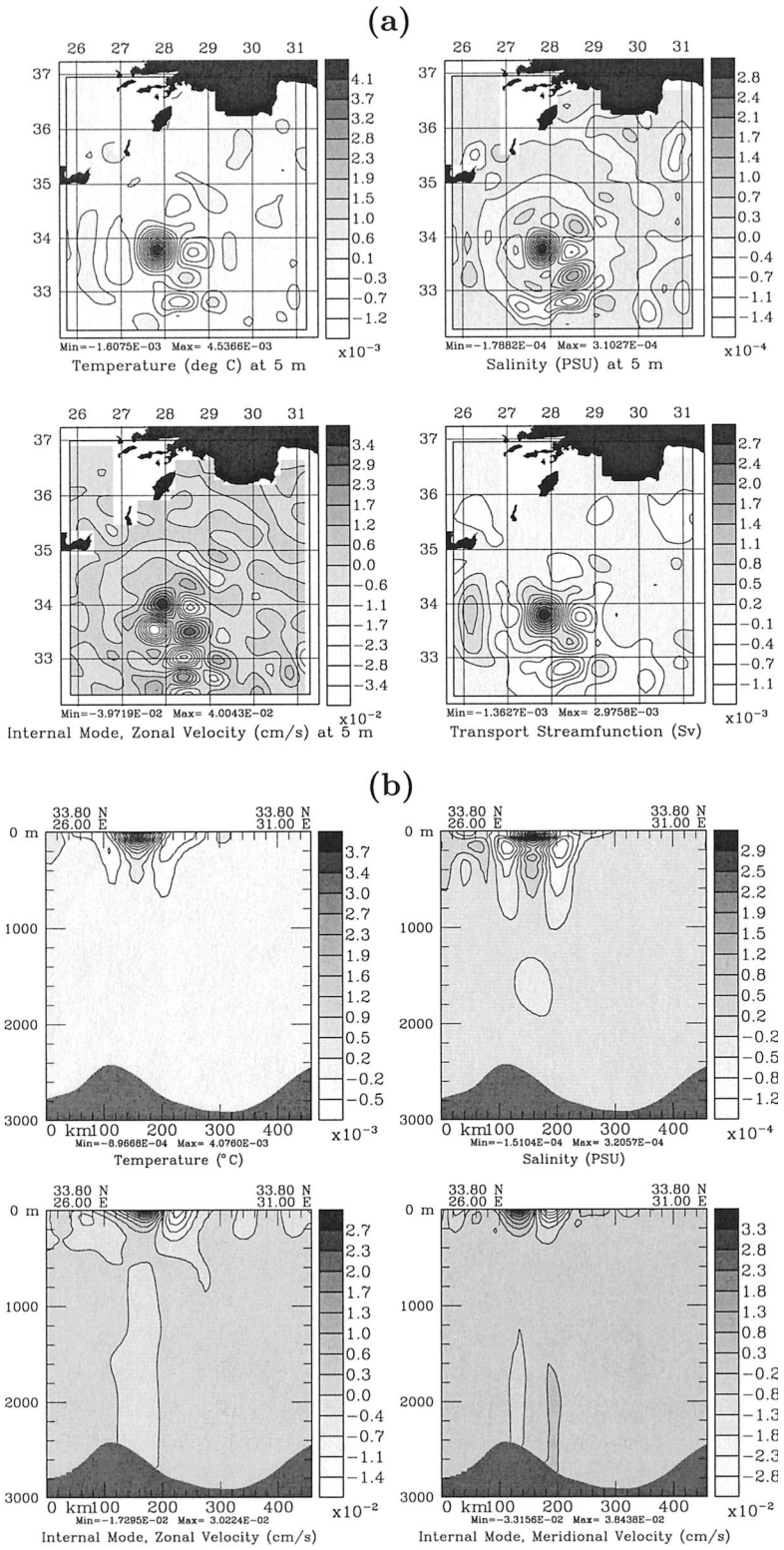

FIG. 20. As Fig. 12 but for the a posteriori covariance functions.

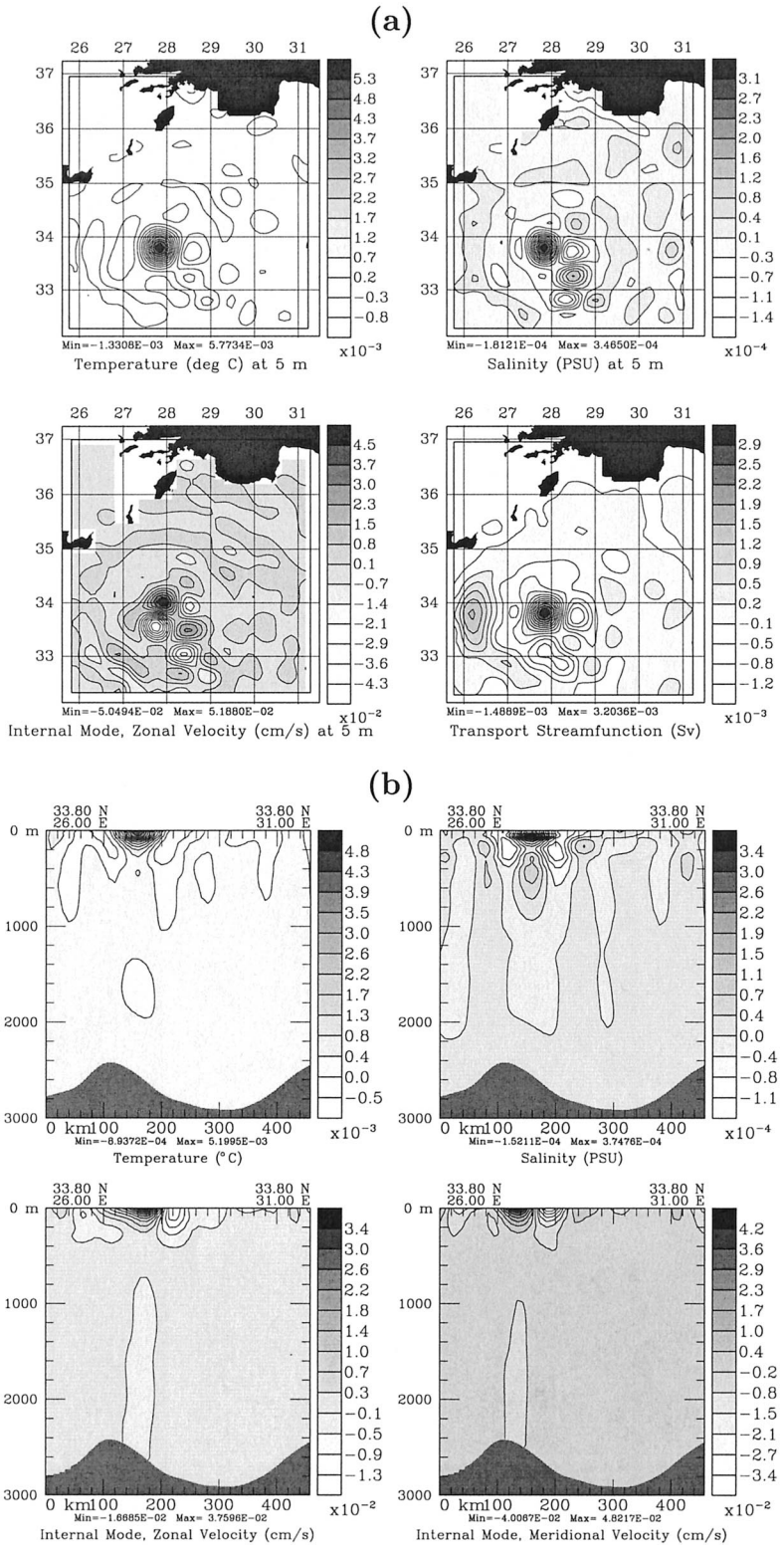

FIG. 21. As Fig. 20 but for case 4.

model (appendix A). At (33.80°N, 27.85°E), both the horizontal and vertical correlation scales have been reduced to small mesoscale values.

Case 2: Horizontal structures (Fig. 20a) clearly show the influences of the low data resolution south of 34°N within 28°–29°E and of the three ship-tracks along 26°E, 26.5°E, and 27°E (Fig. 9a). In the vertical (Fig. 20b), *T*–*T* and *T*–*S* structures have stronger negative lobes and are more surface intensified than a priori (Fig. 12) in part because a priori *T* and *S* data errors are modeled to decay with depths (Fig. 23 in section 5b). The *T*–$\hat{u}$ and *T*–$\hat{v}$ structures have remained similar and surface intensified, but the negative lobe of *T*–$\hat{u}$ is now to the east, in accord with thermal wind effects and lower data resolution in that direction.

Cases 3 and 4: Only case 4 is shown (Fig. 21). Case 3 is analogous, up to amplitudes that are smaller in accord with the global similarity coefficient (Table 2b). In the horizontal (Fig. 21a), structures in case 4 are similar to these in case 2 (Fig. 20a), except that gradients are tighter due to nonlinearities and larger subspace size. In cross-covariances with velocities, differences are largest where features have been shown to be most nonlinear (e.g., Table 3). In the vertical, for all covariances, gradients are tighter than in case 2. Vertical patterns in *T*–$\hat{u}$ and *T*–$\hat{v}$ have remained similar, but these of *T*–*T* and *T*–*S* are more complex, in accord with the additional small mesoscales explained by the vectors 323–400.

5. Quantitative evaluation of fields and impact on forecast performance

The two mapping schemes and three error subspaces (cases 2–4) are now evaluated by measuring the skill of forecasts initialized from the four analyses on 27 March (cases 1–4). Note that for analyses centered on other dates (not shown), results are analogous. Starting from each gridded state (e.g., Figs. 14–16), the numerical PE model is first integrated forward in time. Forecasts are then compared to in situ hydrographic data and satellite sea surface temperature (SST) data. Due to the interactions between tracers and velocities, the effects of the initial flow fields and velocity error subspaces are also assessed.

During 26 March–8 April, in situ samplings are relatively intensive (see Fig. 23a below) and the corresponding CTD profiles are used to evaluate forecasts. The high-resolution satellite images (GISIS 1995) are interpolated onto the numerical model grid, masking cloudy areas. During 27 March–3 April, on 3 days, different halves of the grid are clear and contain limited noise (e.g., Fig. 22a). This leads to a relatively good week composite, even though one should beware of nonsynoptic patching (LLA98). These interpolated day and week images are used to evaluate forecasts.

An issue is that the interval during which forecasts can be compared is limited by the predictive capability of the prediction system. Beyond this limit, nonlinear integrations of data and model errors could reverse conclusions. For the area, period, regime of interest, and data available, the present limit is near 10 days (LER97). Forecasts are thus not compared beyond that. Remaining issues are to define the error and choose its measure. Since comparing forecasts to analyses of data can be misleading, data and forecasts are here directly compared at data points. These data-forecast residuals can be a good estimate of forecast error, in so far as they are larger than the errors in the data. They are measured by root-mean-squares (rms), correlation coefficients, and pattern correlation coefficients (PCC).

a. Satellite SST data

Considering first daily images (e.g., Fig. 22), it is challenging to determine qualitatively which of the forecasts is closest to the satellite SST. Quantitatively, their global scores are indeed similar (see Table 4 below). Focusing on differences, overall, gradients are more accurate in the multivariate 3D scheme (cases 2–4) than in the benchmark (case 1). The branch of the Mid-Mediterranean Jet near 33°N (on Fig. 22a, seen starting at 29°E) is also better represented in cases 2–4 (Figs. 22c–e). The lobes of the Mersa Matruh Gyre are visible in cases 1 and 4 (Figs. 22b,e), but not so much in the cases with the smaller subspace size (Figs. 22c,d). For the Ierapetra and its surrounding cold vortices, cases 1 and 4 have similar large mesoscales. At the small mesoscales, cases 1 and 4 are better than cases 2 and 3; overall, the Ierapetra gradients of case 4 are the most accurate. Comparable comments hold for other daily images (not shown). Considering the week composite (Fig. 30 in LLA98), similar statements can again be made, including for the Rhodes Gyre.

In Table 4, the skill of forecasts generated from the different analyses is evaluated quantitatively. For the three relatively clear days, the correlation coefficient between the satellite SST day composite and estimated 5-m temperature for that day is given (Table 4a). To obtain these coefficients, the horizontal mean of each field is removed first. In Table 4b, the week composite is compared with the week average of the day-to-day 5-m temperature forecasts. To take advantage of the larger composite coverage, two more measures are evaluated: (i) the rms of the residuals between the clear satellite data and averaged forecasts, and (ii) the PCC defined by $\mathrm{PCC} \doteq [\mathbf{T}^S - \mathbf{T}^b)^T(\hat{\mathbf{T}} - \mathbf{T}^b)]/[\|\mathbf{T}^S - \mathbf{T}^b\|_2\|\hat{\mathbf{T}} - \mathbf{T}^b\|_2]$, where the vector $\mathbf{T}^S$ is the satellite week composite, $\hat{\mathbf{T}}$ the estimated week average, and $\mathbf{T}^b$ the background set to the satellite month composite for March 1995. In all computations, only common cloud-free points are considered. For the day snapshots (Table 4a), the main difference is on 27 March: the nowcasts of cases 2–4 are about 15% better than that of the univariate 2D case 1. On other days, a surprising result is that there is little variation among cases. This is mainly due to uncertainties in the satellite data, even though it

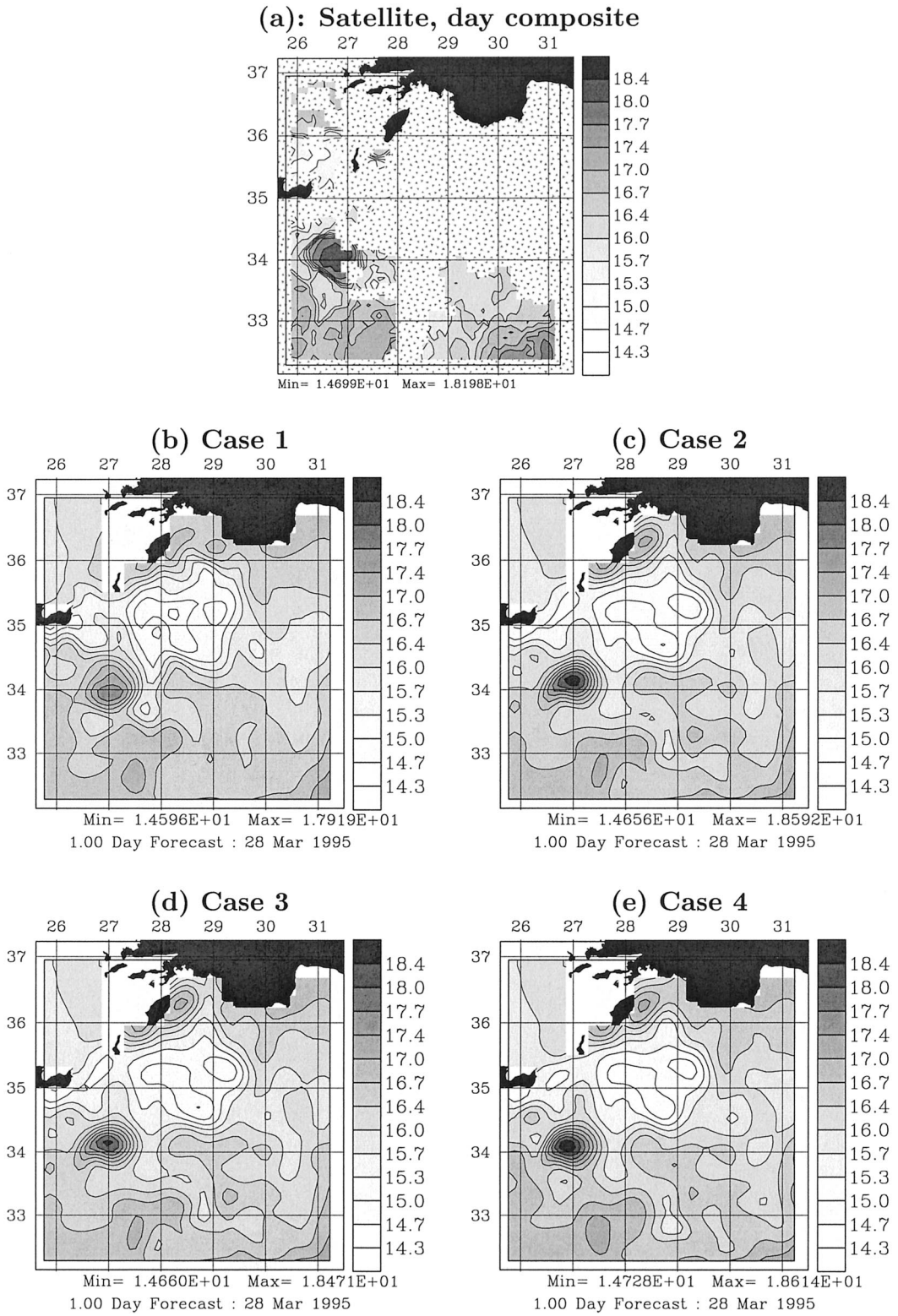

FIG. 22. (a) Satellite SST image for 28 Mar (cloudy areas masked by dots), interpolated on the numerical grid. (b) 1-day forecast of temperature at 5 m for case 1. (c) As (b) but for case 2. (d) As (b) but for case 3. (e) As (b) but for case 4. Note that there is almost no in situ data in the Aegean Sea (Fig. 9a).

TABLE 4. Day and week measures of skill for temperature: Satellite SST vs estimated T fields at 5 m.

a. Day cor coef

Day composite vs	Case	27 Mar nowcast	28 Mar 1-day forecast	3 Apr 7-day forecast
	1	0.57	0.76	0.82
	2	0.67	0.77	0.81
	3	0.67	0.76	0.81
	4	0.66	0.76	0.81

b. Week measures

	Case	Cor coef	PCC	Rms diff
(27 Mar–3 Apr week composite vs average of eight estimated T fields)	1	0.76	0.18	0.3912
	2	0.75	0.20	0.3894
	3	0.75	0.21	0.3870
	4	0.76	0.20	0.3895

also reflects the subspace and forecast convergences. Another artifact of data errors and also varying data coverage is the increasing correlation with time. For the week composite (Table 4b), correlation coefficients are analogous. The PCCs indicate that case 1 is the worst and case 3 the best (adding more vectors can thus at times decrease performance). These PCC numbers are relatively low. This is mainly because they focus on the small mesoscale for which the PCC skill is smaller than for the large mesoscale and subbasin scale due to the initial data resolution. The rms's indicate an error slightly larger for case 1 than for cases 2–4, but variations are not significant (the estimated error in the in situ data at the surface is around 0.3°C, see Fig. 23 below). For the day images, the rms and PCC (not given) lead to the same conclusions. Overall, the satellite data indicate that the skills of cases 2–4 are similar and only a few times slightly larger than the skill of case 1.

b. In situ data

In the evaluations based on in situ *T* and *S* data (Fig. 23a), time is divided in periods of 3 days. For each of these periods, data-forecast residuals are computed at the intersections of the CTDs with the model grid, using the forecast for the center of the period (measurement model details are in LER97). These residuals are measured by rms, averaging level by level. On Fig. 23b, the resulting rms error (rmse) estimates are plotted for the temperature and salinity of cases 1 and 4 on 12 horizontal model levels (from 0 to 500-m depth). Overall, forecast errors increase with forecast durations and decrease with depths in proportion to the variability. For 26–28 March (Rhodes Gyre area) and 29 March–1 April (near 30°E), most rmse's are below the estimated error standard deviations of the data. Both schemes likely lead to good forecasts. Focusing where rmse's are significant, case 4 is better than case 1 at the surface, but the opposite holds near 500 m. For 3–5 April (data along the

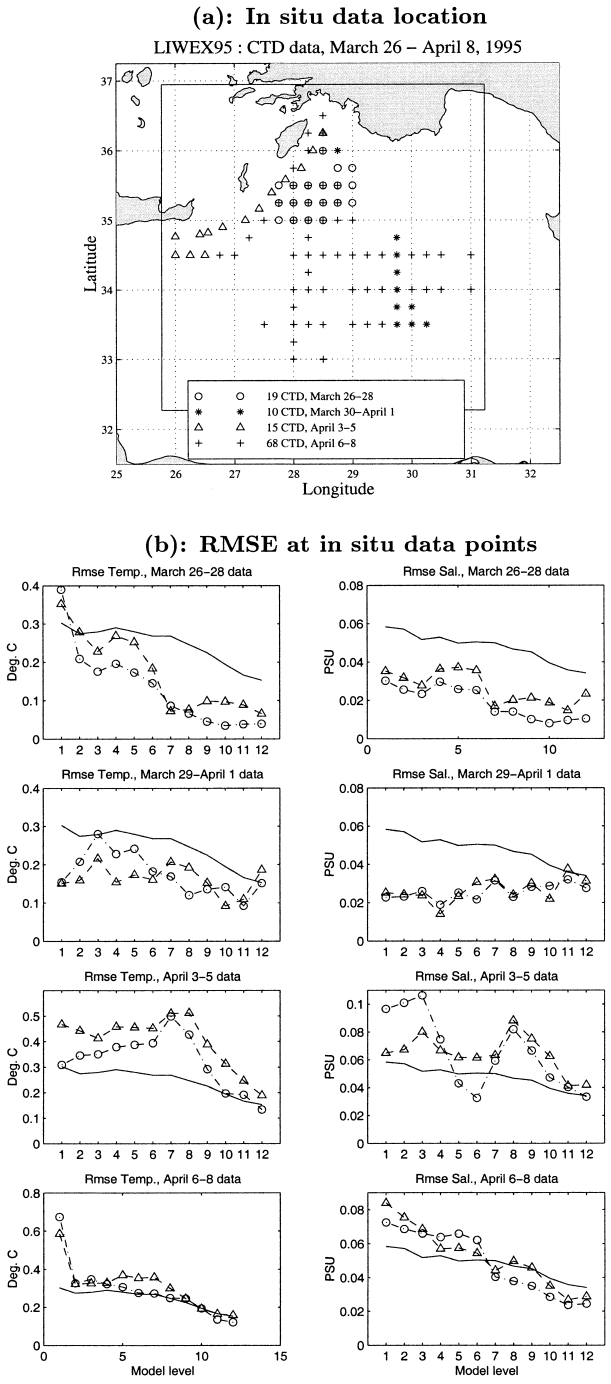

FIG. 23. (a) Sampling locations and total number of CTDs, divided in four 3-day periods. (b) Rmse for (left) temperature and (right) salinity at data points, from horizontal model-level 1 (5 m) to 12 (500 m). Solid line: a priori model of the measurement error standard deviations (LER97). Dash-dotted line with circles: rmse at data point for case 1. Dashed line with triangles: rmse at data point for case 4. Note that scales vary with the 3-day periods. Cases 2 and 3, similar to case 4, are not plotted.

Cretan Arc), rmse's are much larger, in accord with the longer forecast duration and also lesser quality of the numerical model in this region. For *T,* case 1 is better than case 4 at all depths. For *S,* case 4 is substantially better than case 1 in the surface layers, but is worse below. For 6–8 April, at the surface, case 4 is better for *T,* but not for *S.* At middepths, the situation reverses. Near 500 m, case 1 is best but errors become smaller than the estimated data error.

These results first confirm that the two schemes have similar skill. They also restate that the univariate 2D scheme can be too sensitive to small-scale noise (e.g., section 3b), hence the usually lesser skill in the surface layers. They show that the present multivariate 3D scheme can sometimes be less effective at depth. To improve this, either the subspace can be enlarged or the specification of the initial covariance decomposition (appendix A sections a–b) refined. For example, in coastal regions, the lack of better performance at depth is likely due to the initial tracer covariances that were simplified (e.g., horizontally homogeneous, vertically dominated by open-ocean data structures instead of coastal ones).

6. Summary and conclusions

The foregoing study investigated the influence of a priori parameters on the error subspace estimation and mapping methodology introduced in (Lermusiaux et al. 2000, henceforth LAL00). The sensitivities of the subspace and of the a posteriori gridded fields and errors to the size of the subspace, scales considered, and nonlinearities in the dynamical adjustments were exemplified and studied for mesoscale to subbasin-scale physical fields in the northwestern Levantine during 10 February–15 March and 19 March–16 April 1995. A posteriori field and error estimates were evaluated by comparison among each other and by using the univariate 2D analysis scheme of HOPS as a benchmark. Forecasts generated from the various analyses were qualitatively and quantitatively compared to in situ and satellite data. A simple back-of-the-envelope rule for the required size of error subspaces was also outlined and utilized.

Several three-dimensional, multivariate, and multiscale properties were illustrated. The global mapping was shown to estimate simultaneously all physical fields and errors from the tracer data, usefully decompose multivariate covariances, improve vertical correlations and the filtering of environmental noise, yield more accurate field gradients, and lead to velocities that are close to being PE adjusted and a posteriori velocity errors that are PE consistent. In comparison to the geostrophic benchmark, gains were largest where topographic, nonlinear, and diffusion terms mattered. In particular, a posteriori errors were found to reflect complex properties of both the data utilized and the regional dynamics (not always close to geostrophic). Based on the forecasts from the various analyses, the multivariate 3D scheme performed as well as the benchmark. Similar conclusions have been drawn in meteorology (Andersson et al. 1998). Presently, this is likely in part due to the limited data.

Based on sensitivities to scales, for a fixed domain size, smaller scales usually require larger subspaces due to spectral redness. Based on sensitivities to the size of the subspace, truncating the a priori error covariance to a converged subspace is efficient and a priori error eigenvectors of eigenvalues negligible with respect to data errors can be neglected. In the Levantine, increasing the subspace size usually improved the analysis at depths and the small mesoscales. Overall, the variations of a posteriori fields with the parameters of the subspace were as indicated by a global similarity coefficient: if a priori error covariance matrices differed by about 5% (in the standard deviation sense), so did the fields and a posteriori errors. Based on sensitivities to the dynamics of adjustments, it was found however that even when subspaces are globally similar, some of their dominant vectors can be quite different. For example, the nonlinear momentum correction modified the dominant vectors from large-mesoscale variations of the Rhodes Gyre to mesoscale variations of the Ierapetra eddy. It also modified the shape of error spectra, the structures of covariance functions, and some properties of the a posteriori fields and errors. Relative linear–nonlinear differences were computed and as anticipated found to be largest for the features and regions with high shears, around deep eddies or gyres (e.g., Ierapetra, Mersa Matruh Gyre), along fronts (e.g., Mid-Mediterranean Jet), and in Straits. The impacts of inertial oscillations on the subspace adjustment were also discussed.

The study of a priori tracer and velocity variances, spectra of eigenvalues, shapes and amplitudes of dominant multivariate eigenvectors, and structures of (cross)-covariance functions revealed several dynamical properties. The spatial distribution of characteristic hydrographic and velocity scales as well as dominant dynamical balances were quantitatively obtained for most features of the northwestern Levantine. In particular, the Ierapetra eddy was found to be close to gradient–wind balance in the spring of 1995. Coastal-trapped waves were also inferred to be likely along the northern escarpment of the basin and to account for a significant portion of the global variations of momentum and density fields in the region.

Focusing on research directions, a first issue relates to data availability and accurate multiscale statistical models. Mainly for fair comparisons with the univariate 2D scheme but also for lack of sufficient data, a successive correction approach was used instead of a general one for multiple interacting scales. A priori tracer covariance functions were also assumed homogeneous and isotropic in the horizontal instead of being nonhomogeneous and anisotropic in 3D as velocity covariances were. These two assumptions can be removed

in principle (LAL00). In regions with more data than here (to allow accurate fits), the performance of the 3D scheme may then be improved. Another direction concerns algorithms for efficient dynamical adjustment of the error subspace. For example, specific models or processes (e.g., free surface, coupled biochemical irreversibilities, stochastic internal waves) may require specific adjustment procedures. Additional convergence criteria (appendix A) should also be investigated. For example, our experience in other regions suggest that taking into account each variable separately as well as all variables as a whole [Eq. (A22)] is useful. In these criteria, ideal normalizations for specific purposes should also be researched. Most results obtained here apply to the analysis step of data assimilation schemes based on error subspaces. Other research opportunities thus include: error forecasting and adaptive sampling (e.g., Lermusiaux 1999b), model improvements (e.g., LER97), dynamical studies (e.g., Lermusiaux 2001; Lermusiaux and Robinson 2001), and interdisciplinary applications (Robinson and Lermusiaux 2001).

Acknowledgments. I am grateful to Prof. D. G. M. Anderson, Dr. C. J. Lozano, and two anonymous referees for constructive comments on the manuscript, and to Prof. A. R. Robinson, Dr. P. J. Haley, and Mr. W. G. Leslie for their encouragements. I thank the individuals who participated in the LIW95 experiment, the POEM collaboration sponsored by the IOC of UNESCO, Mr. R. Meisner (DLR) for answering questions on the GISIS filtering of the satellite data, and Ms. M. Armstrong for preparing some figures. This work was supported in part by the Office of Naval Research under Grants N00014-95-1-0371, -97-1-0239, and -00-1-0771 to Harvard University.

APPENDIX A

A Priori Error Subspace Estimation and Mapping Methodology

Algorithms introduced in LAL00 for the estimation/initialization of 3D multivariate and multiscale geophysical fields and their dominant errors are summarized. The main step is the construction of the dominant a priori error covariance. The framework is that of continuous–discrete estimation and Ide et al. (1997) is used. The true (superscript ^{t}) state vector $\mathbf{x}^t \in \Re^n$ is assumed subject to the stochastic dynamical and measurement models, respectively,

$$d\mathbf{x}^t = \mathcal{M}(\mathbf{x}^t, t)dt + d\boldsymbol{\eta}^t(t), \quad \text{(A1a)}$$

$$\mathbf{y}^o = \mathcal{H}[\mathbf{x}^t(t_0)] + \boldsymbol{\epsilon}, \quad \text{(A1b)}$$

where $\mathcal{M}$ is the dynamics operator, $\boldsymbol{\eta}^t$ a random process of zero mean and covariance matrix $\mathbf{Q}$, $\mathbf{y}^o \in \Re^m$ the data vector, $\mathcal{H}$ the measurement operator, and $\boldsymbol{\epsilon}$ a random process of zero mean and covariance matrix $\mathbf{R}$. The time t_0 for the estimation is fixed and $\mathbf{R}$ includes a term for data decorrelation with time (see footnote 2 and LER97). An unbiased estimate of $\mathbf{x}^t(t_0)$ is denoted by $\mathbf{x} \in \Re^n$. The state error covariance is defined by $\mathbf{P} \doteq \mathcal{E}\{[\mathbf{x} - \mathbf{x}^t(t_0)][\mathbf{x} - \mathbf{x}^t(t_0)]^{\mathrm{T}}\} \in \Re^{n\times n}$, where $\mathcal{E}\{\cdot\}$ is the statistical mean operator. For the present minimum error variance criterion (section 1), an error subspace of dimension p is the portion of $\Re^n$ that is spanned by the eigenvectors corresponding to the dominant p eigenvalues of a (normalized) error covariance. With this rational reduction, the optimal estimate becomes

$$\left\{\mathbf{x}^a \,\middle|\, \min_{\mathbf{x}} \mathrm{tr}(\mathbf{P}^{a^p}), \text{ knowing } (\mathbf{y}^o, \mathbf{R}) \text{ and } (\mathbf{x}^b, \mathbf{P}^{b^p})\right\}, \quad \text{(A1c)}$$

in which $\mathbf{x}^t(t_0)$ is subject to (A1a)–(A1b). The superscripts $(^b)$ and $(^a)$ refer to estimates before mapping (a priori) and after mapping (a posteriori). The superscript $(^p)$ indicates a rank-p approximation: for example, the a priori/a posteriori principal error covariance $\mathbf{P}^{b^p}/\mathbf{P}^{a^p}$ is the rank-p eigendecomposition of $\mathbf{P}^b/\mathbf{P}^a$. Quantities marked with asterisks are normalized.

a. Observed portions of the a priori error covariance

The value of a field ϕ at location $(\mathbf{r}, z)$, where $\mathbf{r} = (x, y)$ and z are horizontal and vertical positions in a suitable coordinate system, is denoted by $\phi(\mathbf{r}, z)$. The a priori error covariance function for the fields $\phi(\mathbf{r}_1, z_1)$ and $\varphi(\mathbf{r}_2, z_2)$ is then,

$$C_{\phi\varphi}(\mathbf{r}_1, \mathbf{r}_2, z_1, z_2) \doteq \mathcal{E}\{[\phi^b(\mathbf{r}_1, z_1) - \phi^t(\mathbf{r}_1, z_1)][\varphi^b(\mathbf{r}_2, z_2) - \varphi^t(\mathbf{r}_2, z_2)]\}. \quad \text{(A2)}$$

An often efficient representation of (A2) is obtained by expanding the a priori errors into

$$\phi^b(\mathbf{r}, z) - \phi^t(\mathbf{r}, z) = \sum_{i=0}^{\infty} \phi_i(\mathbf{r}) Z^*_{\phi_i}(z), \quad \text{(A3a)}$$

$$\varphi^b(\mathbf{r}, z) - \varphi^t(\mathbf{r}, z) = \sum_{i=0}^{\infty} \varphi_i(\mathbf{r}) Z^*_{\varphi_i}(z), \quad \text{(A3b)}$$

where the $Z^*_{\phi_i}(z)$'s and $Z^*_{\varphi_i}(z)$'s are vertical functions, normalized in some suitable sense. Substituting (A3a)–(A3b) into (A2) yields,

$$C_{\phi\varphi}(\mathbf{r}_1, \mathbf{r}_2, z_1, z_2) = \sum_{i,j=0}^{\infty,\infty} A_{\phi_i,\varphi_j} C^*_{\phi_i,\varphi_j}(\mathbf{r}_1, \mathbf{r}_2) Z^*_{\phi_i}(z_1) Z^*_{\varphi_j}(z_2), \quad \text{(A4a)}$$

where the factor $A_{\phi_i,\varphi_j} = A_{\varphi_j,\phi_i}$ is the horizontal average of $\mathcal{E}\{\phi_i(\mathbf{r})\varphi_j(\mathbf{r})\}$ and $C^*_{\phi_i,\varphi_j}(\mathbf{r}_1, \mathbf{r}_2) \doteq \mathcal{E}\{\phi_i(\mathbf{r}_1)\varphi_j(\mathbf{r}_2)\}^*$ the nondimensional horizontal cross-covariance function associated with ϕ_i and φ_j. The representation (A4a) is efficient if

$$C_{\phi\varphi}(\mathbf{r}_1, \mathbf{r}_2, z_1, z_2) \simeq \sum_{i,j=0}^{I,J} A_{\phi_i,\varphi_j} C^*_{\phi_i,\varphi_j}(\mathbf{r}_1, \mathbf{r}_2) Z^*_{\phi_i}(z_1) Z^*_{\varphi_j}(z_2) \quad \text{(A4b)}$$

with small indices I and J (i.e., A_{ϕ_i,φ_j}'s decay rapidly with increasing i and j).

In section 3c of LAL00, algorithms for estimating the dominant components of error covariance matrices based on the functionals (A4b) are outlined for three types of assumptions involving a single scale, multiple but independent scales, and general multiple scales. In each of these assumptions, the vertical and horizontal decompositions can be obtained either directly from data (EOFs of scale-restricted data residuals) or from an analytical model fit to data (eigendecomposition of a specified covariance matrix).

b. Present construction of the a priori error subspace

Here, the discrete state vector $\mathbf{x} \doteq (\hat{\mathbf{u}}, \hat{\mathbf{v}}, \mathbf{T}, \mathbf{S}, \mathbf{p}) \in \Re^n$ contains gridded values of the $\hat{u}$, $\hat{v}$, T, S, and ψ fields (see footnote 1). The corresponding a priori error covariance estimate, $\mathbf{B}$ (superscript^b omitted), is constructed as follows.

OBSERVED PORTIONS: For the observed T and S, the assumption of multiple but independent scales is made and (A4b) becomes

$$C_{\phi\varphi}(\mathbf{r}_1, \mathbf{r}_2, z_1, z_2) \simeq \sum_{w=0}^{2} R^*_{\phi_w,\varphi_w}(\mathbf{r}_1, \mathbf{r}_2) Z_{\phi_w,\varphi_w}(z_1, z_2), \quad \text{(A5)}$$

for ϕ and φ any four combinations of T and S. As in the univariate 2D scheme, for each scale w in (A5), $R^*_{T_wT_w}$, $R^*_{S_wS_w}$, and $R^*_{T_wS_w}$ are also assumed equal. The tracer submatrix $\mathbf{B}_{\text{trc}}$ of $\mathbf{B}$ is then the sum of Kronecker products of vertical $\mathbf{C}^z_{\text{trc}_w}$ and horizontal $\mathbf{C}^{\mathbf{r}^*}_{\text{trc}_w}$ covariances,

$$\mathbf{B}_{\text{trc}} = \sum_w \mathbf{B}_{\text{trc}_w} = \sum_w \mathbf{C}^z_{\text{trc}_w} \otimes \mathbf{C}^{\mathbf{r}^*}_{\text{trc}_w}. \quad \text{(A6)}$$

The algorithm used here to construct $\mathbf{B}^p_{\text{trc}_w}$ is outlined below (A7)–(A16): for each scale w, $\mathbf{C}^z_{\text{trc}_w}$ is obtained from data (A7)–(A10) and $\mathbf{C}^{\mathbf{r}^*}_{\text{trc}_w}$ from an analytical model fit to data (A11)–(A12). Normalization matrices are denoted by $\mathbf{N}$. They are block-diagonal: for each field, the corresponding element of $\mathbf{N}$ is the sample and spatial averaged variance.

A priori error subspace construction for one scale (w is omitted):
a. Observed portions

Tracer vertical EOFs		
Compute scale-restricted a priori tracer residuals	$\mathbf{d}_i = \mathbf{y}^o_i - \mathcal{H}_i(\mathbf{x}^b), \quad i = 1, \ldots, s.$	(A7)
Remove horizontal average, normalize	$\mathbf{d}^*_i = \mathbf{N}_d^{-1}(\mathbf{d}_i - \overline{\mathbf{d}_i})$.	(A8)
Compute SVD of normalized tracer residuals	$\text{SVD}(\mathbf{S}^*_d \doteq [\mathbf{d}^*_1, \ldots, \mathbf{d}^*_s]) = \mathbf{E}^*_d \mathbf{\Sigma}^*_d \mathbf{V}^{*\text{T}}_d$.	(A9)
Leads to tracer vertical covariance decomposition	$\mathbf{C}^z_{\text{trc}} = \mathbf{E}^z_{\text{trc}} \mathbf{\Pi}^z_{\text{trc}} \mathbf{E}^{z\text{T}}_{\text{trc}}$ where $\mathbf{E}^z_{\text{trc}} = \mathbf{N}_d \mathbf{E}^*_d$ and $\mathbf{\Pi}^z_{\text{trc}} = \mathbf{\Sigma}^{*2}_d/s$.	(A10)
Tracer horizontal covariance eigendecomposition		
Specify normalized covariance from analytical fit	$\mathbf{C}^{\mathbf{r}^*}_{\text{trc}}$ filled from $R^*_{\phi,\varphi}(\mathbf{r}_1, \mathbf{r}_2)$ in (A5).	(A11)
Compute SVD or eigendecompose	$\mathbf{C}^{\mathbf{r}^*}_{\text{trc}} = \mathbf{E}^{\mathbf{r}^*}_{\text{trc}} \mathbf{\Pi}^{\mathbf{r}}_{\text{trc}} \mathbf{E}^{\mathbf{r}^*\text{T}}_{\text{trc}}$.	(A12)
Tracer 3D covariance eigendecomposition		
Based on Kronecker product of (A10) and (A12)	$\mathbf{B}_{\text{trc}} = \mathbf{C}^z_{\text{trc}} \otimes \mathbf{C}^{\mathbf{r}^*}_{\text{trc}}$.	(A13)
Sort eigenproducts $\lambda_z\lambda_r$ and truncate to subspace	p dominant $\lambda_z\lambda_r \Rightarrow$ diagonal $\mathbf{\Pi}_{\text{trc}}$.	(A14)
Construct corresponding 3D eigenvectors	p dominant $\mathbf{e}_z \otimes \mathbf{e}_r \Rightarrow$ rank-p orthogonal $\mathbf{E}_{\text{trc}}$.	(A15)
Result is rank-p decomposition for considered scale	$\mathbf{B}^p_{\text{trc}} = \mathbf{E}_{\text{trc}} \mathbf{\Pi}_{\text{trc}} \mathbf{E}^{\text{T}}_{\text{trc}}$.	(A16)

COMPLETE MULTIVARIATE FORMULATION: The velocity portions of $\mathbf{B}$ are computed through an ensemble of adjustment momentum integrations. The algorithm for a given scale w is outlined below. An ensemble of perturbed tracers $\mathbf{x}^{bj}_{\text{trc}} \doteq (\mathbf{T}^{bj}, \mathbf{S}^{bj})$ is created (A17). The corresponding PE-adjusted velocities are obtained by momentum integrations (A19), starting from unbalanced, for example, geostrophic, initial conditions (A18). Adjusted variability samples are then formed (A20), normalized, and organized by SVD (A21). New adjustments (A17)–(A21) are carried out to increase p until (A22) determines that the number of samples is large enough. Once this occurs, $\mathbf{B}^p$ is obtained (A23). In (A22), the pairs ($\mathbf{E}^*$, $\mathbf{\Pi} = 1/p\ \mathbf{\Sigma}^2$) of rank p and ($\tilde{\mathbf{E}}^*$, $\tilde{\mathbf{\Pi}} = 1/\tilde{p}\ \tilde{\mathbf{\Sigma}}^2$) of rank $\tilde{p} \le p$ correspond to ''new'' and ''previous'' estimates of $\mathbf{B}^p$. With the weighted inner products, $\tilde{\mathbf{\Pi}}^{1/2}\ \tilde{\mathbf{E}}^{*\text{T}}\mathbf{E}^*\ \mathbf{\Pi}^{1/2}$, both principal error directions and amplitudes are compared (other criteria are in LER97). In (A23), $\mathbf{\Gamma}$ is a scaling, block diagonal matrix.

b. Complete primitive equation–based formulation

Form ensemble of perturbed a priori tracer fields	$\mathbf{x}_{\text{trc}}^{b^j} = \mathbf{x}_{\text{trc}}^{b} + \mathbf{E}_{\text{trc}}\mathbf{\Pi}_{\text{trc}}^{1/2}\mathbf{u}^j, \quad j = 1, \ldots, p,$ where here $\mathbf{u}^j = \sqrt{p}\mathbf{e}^j$.	(A17)
Form ensemble of unbalanced a priori state vectors	$\tilde{\mathbf{x}}^{b^j} \doteq (\hat{\mathbf{u}}^b, \hat{\mathbf{v}}^b, \mathbf{x}_{\text{trc}}^{b^j}, \mathbf{p}^b)$.	(A18)
Run p dynamical momentum adjustments	Integrate momentum eqs. in (A1a) with $\mathbf{x}_0 = \tilde{\mathbf{x}}^{b^j}$ and here $\mathbf{x}_{\text{trc}}^{b^j}$ fixed to yield adjusted $\mathbf{x}^{b^j}$.	(A19)
Form differences of PE adjusted fields, normalize	$\mathbf{S}^b \doteq [\mathbf{x}^{b^1} - \mathbf{x}^b; \ldots, \mathbf{x}^{b^q} - \mathbf{x}^b]$; $\mathbf{S}^* = \mathbf{N}^{-1}\mathbf{S}^b$.	(A20)
Compute SVD of rank p	$\text{SVD}_p(\mathbf{S}^b) \doteq \mathbf{N}\ \text{SVD}_p(\mathbf{S}^*) = \mathbf{E}\mathbf{\Sigma}\mathbf{V}^{\text{T}}$; $\mathbf{E} = \mathbf{N}\,\mathbf{E}^*$.	(A21)
Restart (A17)–(A21) and evaluate convergence criterion	$\rho = \dfrac{\sum_{i=1}^{\tilde{p}} \sigma_i(\tilde{\mathbf{\Pi}}^{1/2}\tilde{\mathbf{E}}^{*\text{T}}\mathbf{E}^*\mathbf{\Pi}^{1/2})}{\sum_{i=1}^{p} \sigma_i(\mathbf{\Pi})} \geq \alpha,$ where $\rho \leq 1$, α is a chosen limit $(1 - \epsilon \leq \alpha \leq 1)$ and $\sigma_i(\cdot)$ selects the singular value number i.	(A22)
Result is principal error covariance estimate	$\mathbf{B}^p = \mathbf{\Gamma}\mathbf{E}\mathbf{\Pi}\mathbf{E}^{\text{T}}\mathbf{\Gamma}^{\text{T}}$.	(A23)

c. Error subspace mapping scheme

With $\mathbf{x}^b$, $\mathbf{B}^p$ (A23) and (A1a)–(A1b), the extremum of (A1c) yields the a posteriori estimates $\mathbf{x}^a$, $\mathbf{E}^a$, and $\mathbf{\Pi}^a$, hence $\mathbf{B}^{a^p} \doteq \mathbf{E}^a\mathbf{\Pi}^a\mathbf{E}^{a^{\text{T}}}$. For direct inversion, (A1b) is linearized in the vicinity of $\mathbf{x}^b$ and $\mathbf{x}^a$ is hypothesized to be a linear function of $\mathbf{x}^b$ and $\mathbf{y}^o - \mathcal{H}(\mathbf{x}^b)$, each of which is assumed unbiased. The extremum is then (LER97),

$$\mathbf{x}^a = \mathbf{x}^b + \mathbf{E}\mathbf{\Pi}\mathbf{H}^{p^{\text{T}}}(\mathbf{H}^p\mathbf{\Pi}\mathbf{H}^{p^{\text{T}}} + \mathbf{R})^{-1} \times [\mathbf{y}^o - \mathcal{H}(\mathbf{x}^b)], \tag{A24a}$$

$$\mathbf{U}\mathbf{\Pi}^a\mathbf{U}^{\text{T}} = \tilde{\mathbf{\Pi}}^a \doteq \mathbf{\Pi} - \mathbf{\Pi}\mathbf{H}^{p^{\text{T}}}(\mathbf{H}^p\mathbf{\Pi}\mathbf{H}^{p^{\text{T}}} + \mathbf{R})^{-1}\mathbf{H}^p\mathbf{\Pi}, \tag{A24b}$$

$$\mathbf{E}^a = \mathbf{E}\mathbf{U}, \tag{A24c}$$

where $\mathbf{H}$ is the linearization of $\mathcal{H}$ in the vicinity of $\mathbf{x}^b$, $\mathbf{H}^p \doteq \mathbf{H}\mathbf{E}$, the columns of $\mathbf{U}$ are ordered orthonormal eigenvectors of $\tilde{\mathbf{\Pi}}^a$, and $\mathbf{\Pi}^a$ is diagonal. With the successive corrections, (A24a)–(A24c) are repetitively used for each scale w. The Kalman update and (A24a) differ because of the different gains, $\mathbf{K} \doteq \mathbf{P}^b\mathbf{H}^{\text{T}}(\mathbf{H}\mathbf{P}^b\mathbf{H}^{\text{T}} + \mathbf{R})^{-1}$ and $\mathbf{K}^p \doteq \mathbf{B}^p\mathbf{H}^{\text{T}}(\mathbf{H}\mathbf{B}^p\mathbf{H}^{\text{T}} + \mathbf{R})^{-1}$, respectively. Three cases are discussed in LLA98 as a function of the measurement properties $\mathbf{H}$ and $\mathbf{R}$.

APPENDIX B

Relevant Scalings and Nondimensional Numbers

Table B1 defines numbers that are relevant for the present mesoscale to subbasin-scale study. The notation is standard (Gill 1982; Pedlosky 1987; Cushman-Roisin 1994): g is the acceleration due to gravity; L and D the horizontal and vertical length scales of motion; U and W the horizontal and vertical characteristic velocity scales; f_0 and β_0 the Coriolis parameter and its northward gradient at latitude θ_0; $\rho_s(z)$ the background density profile; and ρ_0 a constant reference density. In addition, $N_s = \sqrt{-(g/\rho_0)(\partial\rho_s/\partial_z)}$ is the Brunt–Väisälä frequency, $R_D = N_sD/f_0$ and $R_{\text{ext}} = \sqrt{gD}/f_0$ the internal and external Rossby radius of deformations, and $\nabla_h H$ the horizontal gradient of bottom topography H. Except for g, all of these characteristic scales are here regional; they are functions of the location and process considered.

TABLE B1. Main nondimensional numbers/parameters.

Number/ parameter	Definition	Ratio
Rossby	$\text{Ro} = \dfrac{U}{f_0 L}$	Relative vorticity to planetary vorticity (also nonlinear advection to Coriolis force)
External Burger	$\text{Bu}_{\text{ext}} = \dfrac{gD}{f_0^2 L^2} = \dfrac{R_{\text{ext}}^2}{L^2}$	Relative vorticity to external vertical vortex-tube stretching (of free surface)
Internal Burger	$\text{Bu} = \dfrac{N_s^2 D^2}{f_0^2 L^2} = \dfrac{R_D^2}{L^2}$	Relative vorticity to internal vertical vortex-tube stretching (of isopycnal surfaces)
Planetary β	$\beta = \beta_0 \dfrac{L^2}{U}$	Planetary (ambient) vorticity gradient to relative vorticity gradient
Topographic β	$\alpha = \lvert\nabla_h H\rvert \dfrac{f_0}{D}\dfrac{L^2}{U}$	Topographic (ambient) vorticity gradient to relative vorticity gradient
Slope or topographic:	$s = \lvert\nabla_h H\rvert \dfrac{L}{D} = \alpha\text{Ro}$	Topographic gradient to motion aspect ratio

For the synoptic and horizontally isotropic quasigeostrophic scales in a stratified ocean, Ro, $\mathrm{Bu}_{\mathrm{ext}}^{-1}$, and $s \ll 1$, but the other numbers may take a range of values: in particular, Bu and α increase with the strength of the stratification and topographic slope, respectively (e.g., Pedlosky 1987). At these scales, using the internal energy (density) equation to estimate W, one can also show that Ro/Bu is the ratio of vertical convergence to horizontal divergence WL/UD, and that the characteristic horizontal variations in density $\Delta\rho$ and vertical variations in background density $\Delta\rho_s$ are related via $\Delta\rho/\rho_0 = (\mathrm{Ro/Bu})(\Delta\rho_s/\rho_0)$.

REFERENCES

Abbott, M. R., and R. M. Letelier, 1998: Decorrelation scales of chlorophyll as observed from bio-optical drifters in the California Current. *Deep-Sea Res.*, **45B,** 1639–1667.

Andersson, E., and Coauthors, 1998: The ECMWF implementation of three-dimensional variational assimilation (3D-Var). III: Experimental results. *Quart. J. Roy. Meteor. Soc.*, **124,** 1831–1860.

Barkmeijer, J., M. Van Gijzen, and F. Bouttier, 1998: Singular vectors and estimates of the analysis-error covariance metric. *Quart. J. Roy. Meteor. Soc.*, **124,** 1695–1713.

Bennett, A. F., and B. S. Chua, 1994: Open-ocean modeling as an inverse problem: The primitive equations. *Mon. Wea. Rev.*, **122,** 1326–1336.

Brenner, S., 1993: Long-term evolution and dynamics of a persistent warm core eddy in the eastern Mediterranean Sea. *Deep-Sea Res.*, **40B,** 1193–1206.

Brink, K. H., 1991: Coastal-trapped waves and wind-driven currents over the continental shelf. *Annu. Rev. Fluid Mech.*, **23,** 389–412.

Carter, E. F., and A. R. Robinson, 1987: Analysis models for the estimation of oceanic fields. *J. Atmos. Oceanic Technol.*, **4,** 49–74.

Chin, T. M., A. J. Mariano, and E. P. Chassignet, 1999: Spatial regression and multiscale approximations for sequential data assimilation in ocean models. *J. Geophys. Res.*, **104C,** 7991–8014.

Cressie, N., and H. C. Huang, 1999: Classes of nonseparable, spatiotemporal stationary covariance functions. *J. Amer. Stat. Assoc.*, **94,** 1330–1340.

Cushman-Roisin, B., 1994: *Introduction to Geophysical Fluid Dynamics.* Prentice-Hall, 320 pp.

Daley, R., 1991: *Atmospheric Data Analysis.* Cambridge University Press, 457 pp.

Dee, D. P., and A. M. da Silva, 1999: Maximum-likelihood estimation of forecast and observation error covariance parameters. Part I: Methodology. *Mon. Wea. Rev.*, **127,** 1822–1834.

De Mey, P., 1997: Data assimilation at the oceanic mesoscale: A review. *J. Meteor. Soc. Japan,* **75,** 415–427.

——, and A. R. Robinson, 1987: Assimilation of altimeter eddy fields in a limited area quasi-geostrophic model. *J. Phys. Oceanogr.*, **17,** 2280–2293.

Derber, J., and F. Bouttier, 1999: A reformulation of the background error covariance in the ECMWF global data assimilation system. *Tellus,* **51A,** 195–221.

Dewar, W. K., and P. D. Killworth, 1995: On the stability of oceanic rings. *J. Phys. Oceanogr.,* **25,** 1467–1487.

Ehrendorfer, M., 1997: Predicting the uncertainty of numerical weather forecasts: A review. *Meteor. Z.,* **6,** 147–183.

Everson, R., P. Cornillon, L. Sirovich, and A. Webber, 1997: An empirical eigenfunction analysis of sea surface temperatures in the western North Atlantic. *J. Phys. Oceanogr.,* **27,** 468–479.

Franke, R., and E. Barker, 2000: Vertical correlation functions for temperature and relative humidity errors. *Mon. Wea. Rev.,* **128,** 3962–3981.

Fukumori, I., and P. Malanotte-Rizzoli, 1995: An approximate Kalman filter for ocean data assimilation: An example with one idealized Gulf Stream model. *J. Geophys. Res.,* **100,** 6777–6793.

Gaspari, G., and S. E. Cohn, 1999: Construction of correlation functions in two and three dimensions. *Quart. J. Roy. Meteor. Soc.,* **125,** 723–757.

Gill, A. E., 1982: *Atmosphere–Ocean Dynamics.* International Geophysics Series, Vol. 30, Academic Press, 662 pp.

GISIS, 1995: User guide for GISIS version 1.0. German Remote Sensing Data Center (DFD), DLR, Issue 0.7, S. White, Ed., 38 pp.

Gneiting, T., 1999: Correlation functions for atmospheric data analysis. *Quart. J. Roy. Meteor. Soc.,* **125,** 2449–2464.

Hamill, T. M., J. S. Whitaker, and C. Snyder, 2001: Distance-dependent filtering of background error covariance estimates in an ensemble Kalman filter. *Mon. Wea. Rev.,* **129,** 2776–2790.

Haney, R. L., R. A. Hale, and C. A. Collins, 1995: Estimating subpycnocline density-fluctuations in the California Current region from upper ocean observations. *J. Atmos. Oceanic Technol.,* **12,** 550–566.

Hecht, A., N. Pinardi, and A. R. Robinson, 1988: Currents, water masses, eddies and jets in the Mediterranean Levantine Basin. *J. Phys. Oceanogr.,* **18,** 1320–1353.

Holland, D. M., and I. T. Webster, 1994: The effects of stratification and alongshore currents on the propagation of coastal-trapped waves. *Contin. Shelf Res.,* **14,** 57–77.

Huthnance, J. M., 1978: On coastal trapped waves: Analysis and numerical calculation by inverse iteration. *J. Phys. Oceanogr.,* **8,** 74–92.

——, 1992: Extensive slope currents and the ocean–shelf boundary. *Progress in Oceanography,* Vol. 29, Pergamon, 161–192.

Ide, K., P. Courtier, M. Ghil, and A. C. Lorenc, 1997: Unified notation for data assimilation: Operational, sequential and variational. *J. Meteor. Soc. Japan,* **75,** 181–189.

Kaplan, A., Y. Kushnir, M. A. Cane, and M. B. Blumenthal, 1997: Reduced space optimal analysis for historical data sets: 136 years of Atlantic sea surface temperatures. *J. Geophys. Res.,* **102** (C13), 27 835–27 860.

Killworth, P. D., J. R. Blundell, and W. K. Dewar, 1997: Primitive equation instability of wide oceanic rings. Part I: Linear theory. *J. Phys. Oceanogr.,* **27,** 941–962.

LeBlond, P. H., and L. A. Mysak, 1971: *Waves in the Ocean.* Elsevier, 602 pp.

Lermusiaux, P. F. J., 1997: Error subspace data assimilation methods for ocean field estimation: Theory, validation and applications. Ph.D. thesis, Harvard University, 402 pp.

——, 1999a: Data assimilation via error subspace statistical estimation. Part II: Middle Atlantic Bight shelfbreak front simulations and ESSE validation. *Mon. Wea. Rev.,* **127,** 1408–1432.

——, 1999b: Estimation and study of mesoscale variability in the Strait of Sicily. *Dyn. Atmos. Oceans,* **29,** 255–303.

——, 2001: Evolving the subspace of the three-dimensional multiscale ocean variability: Massachusetts Bay. *J. Mar. Syst.,* **29,** 385–422.

——, and A. R. Robinson, 1999: Data assimilation via error subspace statistical estimation. Part I: Theory and schemes. *Mon. Wea. Rev.,* **127,** 1385–1407.

——, and ——, 2001: Features of dominant mesoscale variability, circulation patterns and dynamics in the Strait of Sicily. *Deep-Sea Res.,* **48A,** 1953–1997.

——, C. J. Lozano, and D. G. M. Anderson, 1998: On the mapping of multivariate geophysical fields: Studies of the sensitivity to error subspace parameters. Harvard Rep. 58 in Physical/Interdisciplinary Ocean Science, 46 pp.

——, D. G. M. Anderson, and C. J. Lozano, 2000: On the mapping of multivariate geophysical fields: Error and variability subspace estimates. *Quart. J. Roy. Meteor. Soc.,* **126,** 1387–1430.

Lorenc, A. C., 1992: Iterative analysis using covariance functions and filters. *Quart. J. Roy. Meteor. Soc.,* **118,** 569–591.

Louis, A. K., P. Maass, and A. Rieder, 1997: *Wavelets: Theory and Applications.* Wiley and Sons, 342 pp.

Lozano, C. J., A. R. Robinson, H. G. Arango, A. Gangopadhyay, N. Q. Sloan, P. J. Haley, and W. G. Leslie, 1996: An interdisciplinary ocean prediction system: Assimilation strategies and structured data models. *Modern Approaches to Data Assimilation in Ocean Modelling,* P. Malanotte-Rizzoli, Ed., Elsevier Oceanography Series, Vol. 61, Elsevier Science, 413–452.

Malanotte-Rizzoli, P., and Coauthors, 1996: Experiment in eastern Mediterranean probes origin of deep water masses. *EOS, Trans. Amer. Geophys. Union,* **77,** 305–311.

——, B. B. Manca, M. R. d'Alcala, A. Theocharis, S. Brenner, G. Budillon, and E. Ozsoy, 1999: The eastern Mediterranean in the 80s and in the 90s: The big transition in the intermediate and deep circulations. *Dyn. Atmos. Oceans,* **29,** 365–395.

Menemenlis, D., and M. Chechelnitsky, 2000: Error estimates for an ocean general circulation model from altimeter and acoustic tomography data. *Mon. Wea. Rev.,* **128,** 763–778.

Miller, A. J., and B. D. Cornuelle, 1999: Forecasts from fits of frontal fluctuations. *Dyn. Atmos. Oceans,* **29,** 305–333.

Milliff, R. F., and A. R. Robinson, 1992: Structure and dynamics of the Rhodes Gyre System and dynamical interpolation for estimates of the mesoscale variability. *J. Phys. Oceanogr.,* **22,** 317–337.

Mitchell, H. L., and P. L. Houtekamer, 2000: An adaptive ensemble Kalman filter. *Mon. Wea. Rev.,* **128,** 416–433.

Molinari, R. L., and J. F. Festa, 2000: Effect of subjective choices on the objective analysis of sea surface temperature data in the tropical Atlantic and Pacific Oceans. *Oceanol. Acta,* **23,** 3–14.

Molteni, F., R. Buizza, T. N. Palmer, and T. Petroliagis, 1996: The ECMWF ensemble prediction system. Methodology and validation. *Quart. J. Roy. Meteor. Soc.,* **122,** 73–119.

Nittis, K., and A. Lascaratos, 1998: Diagnostic and prognostic numerical studies of LIW formation. *J. Mar. Syst.,* **18,** 179–195.

Özsoy, E., and Coauthors, 1993: A synthesis of the Levantine Basin circulation and hydrography, 1985–1990. *Deep-Sea Res.,* **40B,** 1175–1119.

Pedder, M., and D. Gomis, 1998: Applications of EOF analysis to the spatial estimation of circulation features in the ocean sampled by high-resolution CTD soundings. *J. Atmos. Oceanic Technol.,* **15,** 959–978.

Pedlosky, J., 1987: *Geophysical Fluid Dynamics.* 2d ed. Springer-Verlag, 624 pp.

Rabier, F., A. McNally, E. Andersson, P. Courtier, P. Unden, J. Eyre, A. Hollingsworth, and F. Bouttier, 1998: The ECMWF implementation of three-dimensional variational assimilation (3D-Var). II: Structure functions. *Quart. J. Roy. Meteor. Soc.,* **124,** 1809–1829.

Reichle, R. H., D. B. McLaughlin, and D. Entekhabi, 2002: Hydrologic data assimilation with the ensemble Kalman filter. *Mon. Wea. Rev.,* **130,** 103–114.

Riishojgaard, L. P., 1998: A direct way of specifying flow-dependent background error correlations for meteorological analysis systems. *Tellus,* **50A,** 42–57.

Robinson, A. R., 1996: Physical processes, field estimation and an approach to interdisciplinary ocean modeling. *Earth-Sci. Rev.,* **40,** 3–54.

——, and M. Golnaraghi, 1993: Circulation and dynamics of the eastern Mediterranean Sea: Quasi-synoptic data-driven simulations. *Deep-Sea Res.,* **40B,** 1207–1246.

——, and P. Malanotte-Rizzoli, Eds., 1993: Physical oceanography of the eastern Mediterranean Sea. *Deep-Sea Res., Top. Stud. Oceanogr.,* **40B** (6), 257 pp.

——, and P. F. J. Lermusiaux, 2001: Data assimilation for modeling and predicting coupled physical–biological interactions in the sea. *The Sea,* A. R. Robinson, J. R. McCarthy, and B. J. Rothschild, Eds., Biological–Physical Interactions in the Ocean, Vol. 12, 475–536.

——, ——, and N. Q. Sloan III, 1998: Data assimilation. *The Sea,* K. H. Brink and A. R. Robinson, Eds., The Global Coastal Ocean, Vol. 10, Wiley and Sons, 541–594.

Roether, W., B. B. Manca, B. Klein, D. Bregant, D. Georgopoulos, V. Beitzel, V. Kovačević, and A. Luchetta, 1996: Recent changes in eastern Mediterranean deep waters. *Science,* **271,** 333–335.

Smith, P. C., 1983: Eddies and coastal interactions. *Eddies in Marine Science,* A. R. Robinson, Ed., Springer-Verlag, 446–480.

Thacker, W. C., and R. Lewandowicz, 1996: Climatic indices, principal components, and the Gauss–Markov theorem. *J. Climate,* **9,** 1942–58.

——, and ——, 1997: A comparison of low-dimensional representations of sea-surface temperature anomalies in the North Atlantic. *Int. J. Climate,* **17,** 953–67.

Tippett, M. K., S. E. Cohn, R. Todling, and D. Marchesin, 2000: Low-dimensional representation of error covariance. *Tellus,* **52A,** 533–553.

Toth, Z., and E. Kalnay, 1997: Ensemble forecasting at NCEP and the breeding method. *Mon. Wea. Rev.,* **125,** 3297–3319.

Verron, J., L. Gourdeau, D. T. Pham, R. Murtugudde, and A. J. Busalacchi, 1999: An extended Kalman filter to assimilate satellite altimeter data into a nonlinear numerical model of the tropical Pacific Ocean: Method and validation. *J. Geophys. Res.,* **104C,** 5441–5458.

von Storch, H., and C. Frankignoul, 1998: Empirical modal decomposition in coastal oceanography. *The Sea,* K. H. Brink and A. R. Robinson, Eds., The Global Coastal Ocean, Vol. 10, Wiley and Sons, 419–455.

Wunsch, C., 1997: The vertical partition of oceanic horizontal kinetic energy. *J. Phys. Oceanogr.,* **27,** 1770–1794.